Check for updates

*Advanced Functional Materials*

ADVANCED FUNCTIONAL MATERIALS
www.afm-journal.de

RESEARCH ARTICLE

# Resistive Switching Behavior of Naturally Sourced L-Tryptophan-Based Resistive Random-Access Memory for Multistate Non-Volatile Memory Applications

Moon Ho Lee[1] | Beom Soo Kim[1] | Kunho Moon[1] | Jong Bin An[1,2] | Seok Gyu Hong[1] | Sun Min Song[1] | Hye Jin Son[1] | Jae Seong Han[1] | Hyun Jae Kim[1]

[1]School of Electrical and Electronic Engineering, Yonsei University, Seoul, Republic of Korea | [2]BIT Micro Fab Research Center, Yonsei University, Seoul, Republic of Korea

**Correspondence:** Hyun Jae Kim (hjk3@yonsei.ac.kr)

**Received:** 9 December 2025 | **Revised:** 23 September 2026 | **Accepted:** 5 October 2026

**Keywords:** L-tryptophan | multistate characteristics | natural sources | non-volatile memories | organic materials | resistive random-access memories

## ABSTRACT

Driven by the growing interest in naturally sourced materials for next-generation memory devices, we demonstrate a 6×6 resistive random-access memory (RRAM) crossbar array that utilizes the standard amino acid L-tryptophan (L-trp) as the active layer. The indole ring of L-trp facilitates trap sites, while its carboxylic acid group enables the formation of a crucial aluminum oxide interfacial layer via reaction with the Al top electrode. The Al/L-trp/W structured RRAM exhibits reliable bipolar resistive switching with an on/off ratio of $1.94 \times 10^4$, endurance of over 1000 cycles, and stable retention characteristics for $10^5$ s. Furthermore, the multistate characteristics of the L-trp-based RRAM are confirmed by achieving 12 distinguishable resistance states through compliance current modulation from 0.5 to 100 mA. Quantitative analysis demonstrates a minimum adjacent resistance ratio of 1.98, ensuring high state separability. This successful demonstration of 12 distinguishable resistance states in the L-trp-based RRAM highlights the significant potential of L-trp in next-generation memory devices.

## 1 | Introduction

The exponential growth of data-driven technologies, such as artificial intelligence and Internet of Things, has generated an unprecedented demand for high-density, low-power memory devices. Although conventional silicon-based memory devices have served as the backbone of the digital revolution, they face significant environmental concerns, including high-energy fabrication processes and increased in electronic waste containing hazardous materials. Therefore, the development of next-generation memory technologies based on naturally sourced materials that are amenable to low-energy, straightforward fabrication processes is not merely an alternative, but also a critical imperative for next-generation memory devices [1–7].

Among the various next-generation memory candidates, resistive random-access memory (RRAM) is a highly promising technology owing to its simple metal-insulator-metal structure, fast switching, high endurance, and low power consumption [8–10]. However, most RRAM research has focused on inorganic materials and oxides, which are non-naturally sourced materials [11–14]. These materials are often toxic, hindering efforts to minimize electronic waste. Therefore, the development of naturally sourced material-based RRAM is imperative to reduce electronic waste [15].

To date, naturally sourced materials explored as RRAM active layers can be broadly categorized into four classes: saccharides, proteins, nucleic acids, and plant-derived materials.

All rights reserved, including rights for text and data mining and training of artificial intelligence technologies or similar technologies.
© 2026 Wiley-VCH GmbH

Saccharide-based RRAM, including monosaccharides such as glucose and fructose, disaccharides such as lactose and lactulose, and polysaccharides such as starch, cellulose, chitosan, nitrocellulose, and pectin has demonstrated bipolar resistive switching with on/off ratios ranging from ~$10^2$ to ~$10^7$ [16–24]. However, saccharide-based materials generally lack aromatic functional groups, limiting the density of available trap sites and thereby constraining multilevel switching capability. Protein-based RRAM, the most extensively studied category, includes silk fibroin, sericin, gelatin, egg albumen, keratin, and collagen, but these macromolecular systems inherently suffer from compositional heterogeneity, leading to significant device-to-device variability [25–30]. Moreover, achieving competitive performance in many protein-based RRAM devices requires metal nanoparticle doping or inorganic hybrid synthesis, which introduces process complexity. DNA-based RRAM has demonstrated multistate memory behavior, although most studies rely on metal ion intercalation for enhanced switching [31]. Plant-derived RRAM using crude botanical extracts such as lotus leaf, dead leaf, and sweet potato peel has shown the feasibility of minimally processed materials, yet the compositional complexity of these extracts makes it challenging to identify the active switching component [32–34]. Notably, proteins, plant-derived materials, and DNA are all high-molecular-weight macromolecules containing numerous functional groups, making it inherently difficult to determine which specific moiety governs the resistive switching mechanism and thereby limiting rational device optimization.

Accordingly, while RRAM based on naturally sourced materials has been reported repeatedly, it still faces significant challenges, including poor operational reliability and stability [35, 36]. To overcome these limitations, many studies have attempted to create new composite materials by doping naturally sourced materials with metals or synthesizing them with other materials [37, 38]. Nevertheless, this approach involves complex material synthesis, which paradoxically negates the key advantage of a simple fabrication process. Therefore, it is essential to develop a naturally sourced material-based RRAM that achieves high operational reliability and stability by leveraging only the intrinsic properties of these materials, without adding process complexity.

In addition to the high operational reliability and stability of naturally sourced material-based RRAM, it is essential to achieve stable multilevel operation, enabling multiple resistance states to be stored in a single memory cell. These multi-level operations in a single memory cell maximize the potential of next-generation memory devices, enabling high density and circuit simplification [39]. This technology not only overcomes the density limitations of current memory, but also plays a pivotal role in building brain-inspired neuromorphic computing systems that process information by representing various connection strengths, similar to human brain synapses. Therefore, ideal materials for next-generation memory devices should be naturally sourced, exhibit high reliability and stability, and possess multistate characteristics through gradual fine-grained modulation.

In this context, amino acids represent a promising yet unexplored class of naturally sourced materials for RRAM active layers. Despite being the fundamental building blocks of proteins, no pure single amino acid has been demonstrated as a standalone RRAM active layer to date; only L-cysteine has been explored, and solely in the form of a Ti–L-cysteine molecular layer deposition hybrid—not as a pure amino acid film [40]. Amino acids possess several intrinsic advantages that make them attractive candidates for RRAM applications. First, amino acids contain a carboxylic acid group (–COOH) that, analogous to the hydroxyl groups in saccharides, can react with reactive metal electrodes such as Al to form a thin metal-oxide interfacial layer essential for conductive filament formation and rupture. Second, amino acids in the solid state adopt a zwitterionic structure ($NH_3^+/COO^-$) with an inherently large permanent dipole moment (~14–16 D), which—if preferentially oriented during film formation—may generate a local built-in electric field that facilitates charge transport and lowers the operating voltage. This possibility is supported by the demonstrated ferroelectricity in $\gamma$-glycine crystals, where aligned zwitterionic dipoles produce a macroscopic switchable polarization [41]. These intrinsic properties—interfacial oxide formation capability and zwitterionic dipole character—collectively suggest that amino acids are well-suited as RRAM active-layer materials warranting systematic investigation.

In this study, we propose an RRAM using the standard amino acid L-tryptophan (L-trp) as the active layer and systematically analyze its characteristics. L-trp is a particularly attractive, naturally sourced material for the active layer of multistate RRAM. L-trp is an essential amino acid for humans and is inherently naturally sourced. Additionally, among the 20 standard amino acids, L-trp is uniquely suited for RRAM applications because it is the only amino acid that possesses an indole ring as its side chain—a bicyclic aromatic heterocycle formed by the fusion of a pyrrole ring and a benzene ring. As shown in Figure S1, this indole ring constitutes the largest $\pi$-conjugated system (10 $\pi$-electrons delocalized across 9 atoms plus one nitrogen lone pair) among all amino acid side chains, far exceeding the benzene ring, phenol ring, and imidazole ring (each with 6 $\pi$-electrons) [42–44]. This extended $\pi$-conjugated system provides three critical advantages for RRAM device operation. First, the $\pi$-conjugated system intrinsically acts as a charge-trapping site, and the extended $\pi$-conjugated system of the indole ring provides the highest density of trap sites among all amino acid side chains. This abundant trap density enables stable charge capture, which directly enhances the data retention characteristics. Second, the extended 10 $\pi$-electron conjugated system yields the smallest HOMO–LUMO energy gap among the standard aromatic amino acids, as evidenced by indole's ionization energy of 7.9 eV compared to 9.24 eV for the benzene ring and 8.49 eV for the phenol ring [45]. This reduced energy gap lowers the barrier for charge injection and trap-to-trap hopping, enabling switching at relatively low operating voltages. Third, under repeated electrical stress during switching cycles, the indole ring can stabilize radical intermediates through extensive spin delocalization across the entire bicyclic $\pi$-system; the L-trp radical is well-characterized in biochemistry, with unpaired spin density broadly distributed over the N1, C3, C5, and C7 positions, enabling reversible charge-state cycling that supports high device endurance [46, 47]. This radical stabilization mechanism is analogous to the principle demonstrated in Ru-azo aromatic RRAM, where stable, reversible ligand radical formation via $\pi$-delocalization enabled ~$10^{12}$ switching cycles [48]. Furthermore, L-trp exhibits a high thermal decomposition temperature of ~289°C, which exceeds gelatin (~200–230°C) and egg albumen (~220–250°C), providing additional resistance to Joule-heating-induced degradation



16163028, 2026, 92, Downloaded from https://advanced.onlinelibrary.wiley.com/doi/10.1002/adfm.78971 by Yonsei University Library, Wiley Online Library on [22/11/2026]. See the Terms and Conditions (https://onlinelibrary.wiley.com/terms-and-conditions) on Wiley Online Library for rules of use; OA articles are governed by the applicable Creative Commons License

during repeated device operation. These structural and thermal features are expected to contribute to the high performance, stability, and multistate characteristics of the L-trp-based RRAM.

Therefore, herein, the bipolar resistive switching (BRS) of the L-trp-based RRAM was investigated by controlling the applied dual-voltage sweep and the compliance current ($I_{CC}$). To understand the operating mechanism of BRS in the L-trp-based RRAM, various analyses were performed, including Fourier transform infrared (FT-IR) spectroscopy, atomic force microscope (AFM), transmission electron microscopy (TEM), energy-dispersive X-ray spectroscopy (EDS), and X-ray photoelectron spectroscopy (XPS). Finally, the potential for multistate operation in L-trp-based RRAM was evaluated using BRS operations under $I_{CC}$ modulation.

## 2 | Results and Discussion

Figure 1a illustrates the fabrication process of the L-trp-based RRAM. First, a W bottom electrode was deposited onto the prepared substrate by sputtering using a shadow mask. W was selected as the bottom electrode because of its high thermal stability and lower reactivity toward the L-trp active layer than the top electrode. Subsequently, the prepared L-trp solution was spin-coated onto the W bottom electrode-deposited substrate to form an L-trp active layer. Annealing was performed on a hot plate to remove the residual solvent and solidify the L-trp active layer. Finally, an Al top electrode was deposited through a shadow mask using an e-beam evaporator, completing the L-trp-based RRAM with a crossbar array structure. Al was selected because of its high reactivity with the L-trp active layer. The detailed process conditions are described in the *Experimental Section*. A photograph of the actual fabricated device and a digital microscope image of its individual memory cells are presented in Figure S2.

To verify that the chemical structure of the L-trp active layer was stably maintained during the fabrication process, FT-IR analysis was performed. Figure 1b shows the spectrum of the L-trp powder, and Figure 1c shows the spectrum of the L-trp active layer formed as a film after spin-coating and annealing. To ensure a valid comparison, both the powder and the film were measured in attenuated total reflectance (ATR) mode on the same FT-IR instrument under identical conditions (4000–400 $cm^{-1}$, 4 $cm^{-1}$ resolution). The film was prepared under the same spin-coating and annealing conditions as the device active layer, so that the two spectra are directly comparable without any measurement-mode discrepancy. First, the peak at ~1700 $cm^{-1}$, which corresponds to the neutral carboxylic acid, is absent in both the powder and film spectra. In contrast, the peaks at ~1591 and ~1414 $cm^{-1}$, which correspond to the carboxylate ion, are observed in both the powder and film spectra. This indicates that the carboxylic acid group in L-trp exists in an ionic rather than a neutral state. These highly reactive carboxylate ions are expected to play a crucial role in the interfacial reaction with the top electrode and in the memory switching mechanism. Furthermore, the peak at ~3403 $cm^{-1}$, which corresponds to the ammonium group, and the peaks at ~3078 and ~744 $cm^{-1}$, which correspond to the indole ring, are observed in both the powder and film spectra [49]. Here, the indole ring is expected to function as an independent trap site [50]. The presence of these peaks in both the powder and film indicates that the spin-coating and annealing processes had a minor impact on the chemical structure of L-trp.

While all characteristic peaks of L-trp are commonly observed in both the powder and the film, a secondary difference is noted in the peak shapes, as the peaks in the L-trp film are generally sharper and more clearly resolved than those in the L-trp powder. In particular, a peak at ~2915 $cm^{-1}$, which is not distinguishable in the L-trp powder spectrum owing to overlap with the broad N–H stretching band centered at ~3403 $cm^{-1}$, becomes clearly discernible in the L-trp film spectrum. Here, the peak at ~2915 $cm^{-1}$ signifies the aliphatic C—H bonds in the side chain of L-trp. Since these aliphatic C—H bonds are intrinsic to the L-trp molecule and are therefore present in both forms, the appearance of this peak reflects the narrowing of the overlapping band rather than the formation of any new chemical bond. Additionally, the peak at ~744 $cm^{-1}$ was observed to be sharper in the L-trp film compared to that in the L-trp powder. This suggests that, unlike the randomly aggregated state in the powder, the L-trp molecules in the spin-coated film experience a more uniform local chemical environment, resulting in enhanced short-range conformational uniformity. It should be noted that this peak sharpening reflects homogenization of the local molecular environment during the dissolution–redeposition process, rather than any change in the chemical structure itself or long-range crystallographic ordering, as FT-IR spectroscopy probes vibrational modes sensitive to local conformational and hydrogen-bonding environments but cannot directly resolve long-range structural periodicity.

To further assess the film morphology, AFM analysis was performed on the L-trp films. Figure 1d,e presents 3D AFM topography images, and the corresponding 2D AFM images are provided in Figure S3. The L-trp film with 24 h aged solution exhibits a root-mean-square surface roughness ($R_q$) of 0.197 nm, which is comparable to the values reported for well-established smooth spin-coated organic films such as PMMA (~0.18 nm) and polystyrene (~0.2 nm), and falls within the range of 0.10–0.25 nm reported for optimized spin-coated polymer films [51–53]. In contrast, the L-trp film without 24 h aged solution—in which incomplete dissolution of L-trp in dimethyl sulfoxide (DMSO) promotes molecular aggregation during film formation—exhibits a significantly higher $R_q$ of 0.927 nm with clearly visible surface aggregation features. The surface roughness of the L-trp film without 24 h aged solution approaches the threshold (~1 nm) above which aggregation-induced morphological degradation has been reported to compromise device performance in organic thin-film devices [54]. These results confirm that the spin-coating process produces a highly uniform and continuous L-trp thin film with sub-nanometer surface roughness, which ensures homogeneous active-layer thickness across the device area and provides a reliable foundation for achieving reproducible resistive switching characteristics.

Depending on numerous previous studies on RRAM using organic active layers, the resistive switching characteristics are predominantly governed by the formation and rupture of conductive filaments (CFs) within a thin metal-oxide interfacial layer formed at the interface between the organic active layer and the top electrode [55–57]. Accordingly, in this context, TEM and EDS mapping analyses were performed to directly observe the



16163028, 2026, 92, Downloaded from https://advanced.onlinelibrary.wiley.com/doi/10.1002/adfm.78971 by Yonsei University Library, Wiley Online Library on [22/11/2026]. See the Terms and Conditions (https://onlinelibrary.wiley.com/terms-and-conditions) on Wiley Online Library for rules of use; OA articles are governed by the applicable Creative Commons License

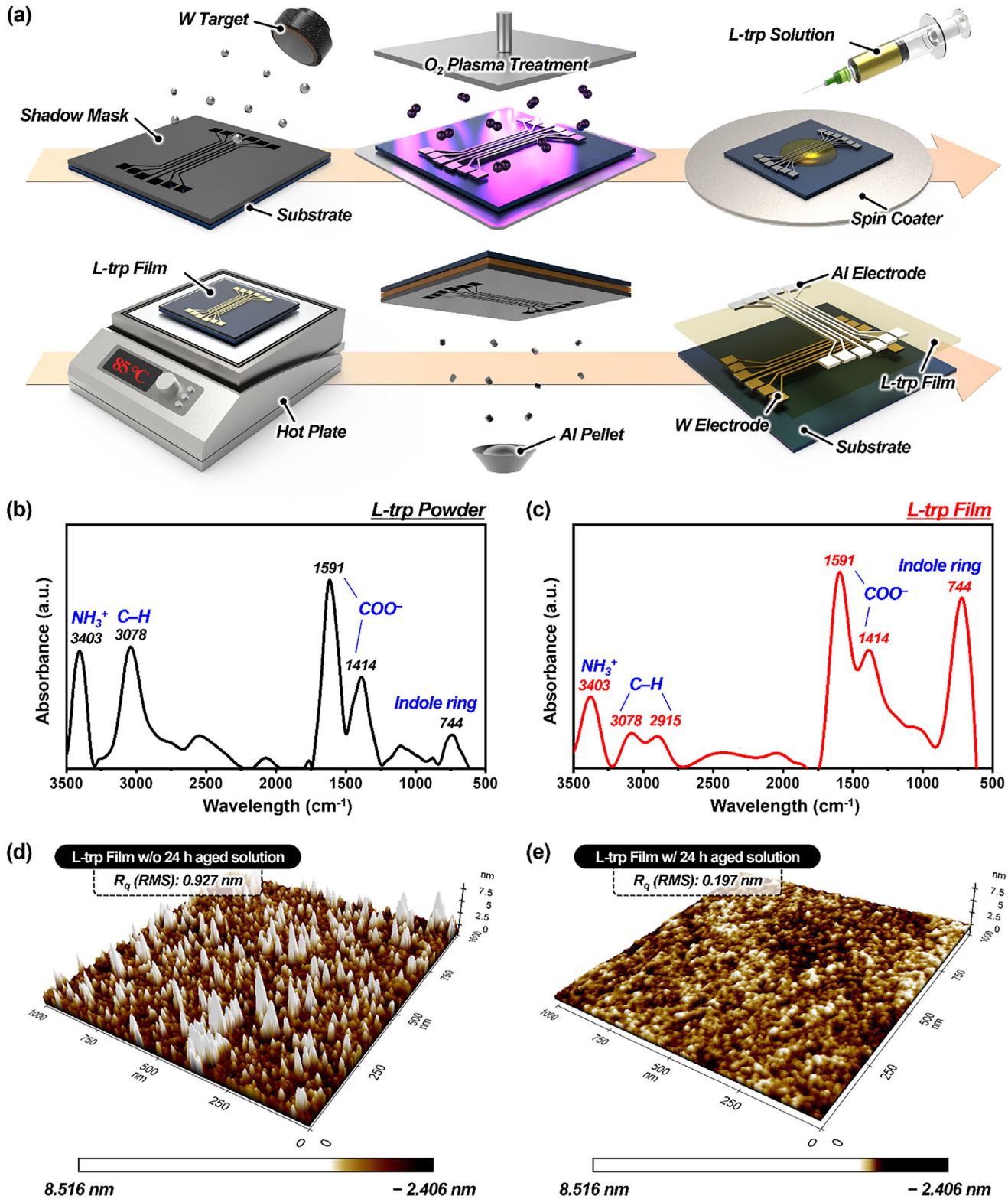



**FIGURE 1** | Fabrication process and active layer characterization. (a) Schematic illustration of the L-trp-based RRAM fabrication process, FT-IR spectra of the L-trp (b) powder and (c) film, and 3D AFM images of the L-trp film prepared (d) without 24 h aged solution showing surface aggregation with $R_q = 0.927$ nm and (e) with 24 h aged solution showing a smooth, uniform surface with $R_q = 0.197$ nm.



16163028, 2026, 92, Downloaded from https://advanced.onlinelibrary.wiley.com/doi/10.1002/adfm.78971 by Yonsei University Library, Wiley Online Library on [22/11/2026]. See the Terms and Conditions (https://onlinelibrary.wiley.com/terms-and-conditions) on Wiley Online Library for rules of use; OA articles are governed by the applicable Creative Commons License

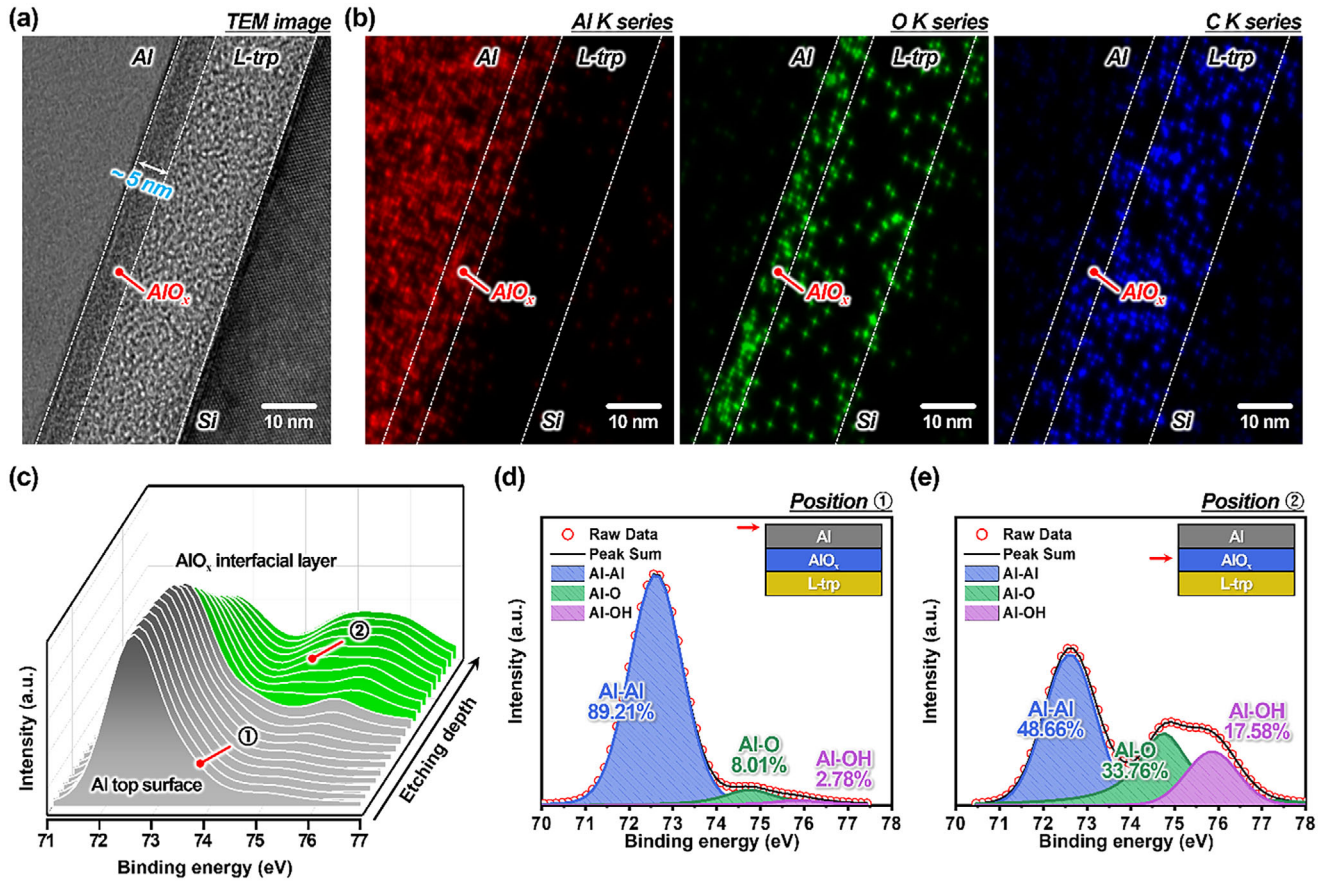



**FIGURE 2** | Structural and chemical characterization of the Al/L-trp interface. (a) Cross-sectional TEM image showing the interfacial layer and (b) corresponding EDS mapping of Al, O and C elements. (c) XPS depth profile and Al 2p XPS spectra from the (d) Al top electrode and (e) Al/L-trp interface, respectively.

interface between the L-trp active layer and the Al top electrode in the L-trp-based RRAM. Notably, Al is a reactive metal that is prone to oxidation because of its relatively low standard electrode potential of −1.66 V [58, 59]. Furthermore, as confirmed by the FT-IR analysis, the L-trp active layer contains a large amount of highly reactive carboxylate ions. Therefore, these ions are expected to react with the Al top electrode during the deposition process to form a metal-oxide interfacial layer.

This expectation was confirmed by the cross-sectional TEM image in Figure 2a, which distinctly shows a 5-nm-thin interfacial layer between the Al top electrode and the L-trp active layer. To identify the chemical composition of this interfacial layer, EDS mapping was conducted (Figure 2b), which confirmed the concentrated distribution of Al and O in this region and clearly demonstrated that the thin film is an aluminum oxide ($AlO_x$) interfacial layer. For reference, the EDS mapping of Si is shown in Figure S4.

XPS analysis was performed further verify the presence of the $AlO_x$ interfacial layer at the Al/L-trp interface, as identified by TEM and EDS mapping, and to characterize its chemical bonding in detail. Figure 2c shows the XPS depth profile, illustrating the elemental distribution as a function of depth. This enabled precise identification of the positions at the Al top surface (position 1) and the Al/L-trp interface (position 2). Figure 2d,e shows the Al 2p spectra at positions 1 and 2, respectively. Each spectrum was deconvoluted into Al–Al, Al–O, and Al–OH peaks at 72.5 ± 0.2, 74.4 ± 0.2, and 75.2 ± 0.2 eV [60].

As expected, at the Al top surface (position 1), the metallic Al–Al peak was predominant, accounting for 89.21%, whereas the Al–O and Al–OH peaks were merely at 8.01% and 2.78%, respectively. However, a dramatic change in the chemical bonding was observed at the Al/L-trp interface (position 2). The proportion of the Al–Al peak significantly decreased to 48.66%, whereas the Al–O peak increased to 33.76% and the Al–OH peak increased to 17.58%. This increase in the relative proportions of the Al–O and Al–OH components at position 2, compared to those at position 1, provides definitive chemical evidence that the Al reacted with carboxylate ions and other residual groups within the L-trp layer to form an $AlO_x$ interfacial layer. The existence of a naturally formed $AlO_x$ interfacial layer at the Al/L-trp interface was structurally and chemically verified by TEM, EDS spectroscopy, and XPS. This $AlO_x$ interfacial layer serves as the key region where CFs form and rupture during the resistive switching mechanism.

Based on the $AlO_x$ interfacial layer, confirmed by the preceding analyses, the electrical memory characteristics of the fabricated L-trp-based RRAM were evaluated. For reference, solutions were prepared using deionized (DI) water and DMSO as solvents to



16163028, 2026, 92, Downloaded from https://advanced.onlinelibrary.wiley.com/doi/10.1002/adfm.78971 by Yonsei University Library, Wiley Online Library on [22/11/2026]. See the Terms and Conditions (https://onlinelibrary.wiley.com/terms-and-conditions) on Wiley Online Library for rules of use; OA articles are governed by the applicable Creative Commons License

optimize electrical memory characteristics. Optimal electrical memory characteristics were obtained by examining the *I–V* characteristics of L-trp-based RRAM fabricated from solutions in which the L-trp powder was completely dissolved. The solution images, depending on the solvent and concentration, and their respective *I–V* characteristics, are shown in Figures S5 and S6. Table S1 summarizes the electrical characteristics of L-trp-based RRAM fabricated with solutions using various solvents and concentrations. To ensure statistical reliability, three 6×6 crossbar arrays were fabricated for each of the four conditions (3 arrays × 36 devices = 108 devices per condition), and the thickness, on/off ratio, set voltage ($V_{SET}$) and reset voltage ($V_{RESET}$) were measured to ensure statistical reliability. The device-to-device statistics are summarized in Figure S7.

The L-trp film thickness increases systematically with L-trp powder concentration. The performance variations across conditions can be attributed to the interplay between the film thickness and the density of indole ring trap sites within the L-trp active layer. The $AlO_x$ interfacial layer is excluded from this interplay because it forms through a surface-confined reaction between the topmost carboxylate groups and the Al top electrode, so that its formation is essentially independent of the total active-layer thickness. Indeed, cross-sectional TEM and EDS mapping confirm that an $AlO_x$ interfacial layer of ∼5 nm is consistently formed for L-trp active layers of 13 and 29 nm as shown in Figure S8, comparable to that of the 20 nm active layer (Figure 2a). For the DI water 1 wt.% condition, incomplete dissolution of L-trp in DI water results in residual powder aggregation within the film, and the proximity of the DI water boiling point (100°C) to the annealing temperature (85°C) prevents complete solvent removal, introducing electrical noise and degrading device uniformity. For the DMSO 1 wt.% condition, although DMSO enables complete dissolution, the low concentration yields an excessively thin film of ∼13 nm, which cannot adequately suppress the leakage current between the electrodes, elevating the HRS current and precluding stable resistive switching. For the DMSO 3 wt.% condition, the excessively thick film of ∼29 nm provides an over-abundance of indole ring trap sites; the saturated trap sites cannot release the trapped electrons during the reset process, explaining the absence of a clear reset process despite a moderate on/off ratio of $\sim 10^3$. A quantitative analysis of the trap density and its role in the conduction mechanism is provided later.

In contrast, the L-trp-based RRAM fabricated using the 2 wt.% DMSO solution not only exhibited clear bipolar resistive switching characteristics, but also exhibited a high on/off ratio of $1.94 \times 10^4$ with tight device-to-device distributions across all metrics. This condition provides an optimal L-trp film thickness of ∼20 nm that adequately suppresses the leakage current between the electrodes while providing a sufficient indole ring trap density for clear high-resistance state (HRS) and low-resistance state (LRS) separation. Therefore, this condition was selected as optimal.

To further investigate the effect of the L-trp active layer thickness on the device characteristics, L-trp-based RRAM devices were fabricated at six spin-coating speeds (1000, 2000, 3000, 4000, 5000, and 6000 rpm) using the optimized 2 wt.% DMSO solution. As shown in Figure S9, the L-trp film thickness decreases systematically from 33.21 nm at 1000 rpm to 13.93 nm at 6000 rpm, and the measured *I–V* characteristics and key electrical parameters for each condition are summarized in Figure S10 and Table S2. For excessively thick films at low spin-coating speeds (1000–2000 rpm), the initial current and HRS current are significantly reduced due to the increased resistance of the thicker organic layer; however, the over-abundance of indole ring functional groups provides an excessive density of charge trap sites, preventing the release of trapped electrons during the reset process. Moreover, the insufficient centrifugal force at these low speeds degrades the surface uniformity of the L-trp film, resulting in non-uniform thickness distribution that further contributes to the incomplete switching behavior. Conversely, for excessively thin films at high spin-coating speeds (4000–6000 rpm), the reduced film thickness leads to increased leakage currents and elevated initial/HRS currents, while the insufficient density of indole ring trap sites degrades the charge storage capability essential for clear HRS/LRS separation. The optimized condition of 3000 rpm provides the optimal balance between leakage current suppression, trap site density, and film surface uniformity, yielding the highest on/off ratio and the stable bipolar resistive switching characteristics among all spin-coating speed conditions.

Figure 3a shows the forming processes, which activates the L-trp-based RRAM from an insulating state to a switchable state by applying electrical bias, and the subsequent reset process. At an $I_{CC}$ of 0.5 mA, soft breakdown occurred at a forming voltage ($V_{FORM}$) of approximately 4.28 V in the positive bias region, as indicated by a sharp increase in current that switched the L-trp-based RRAM from HRS to LRS. Subsequently, a reset process was observed in the L-trp-based RRAM, switching to the HRS at a $V_{RESET}$ of approximately −1.27 V under negative bias.

After the forming and reset process, the L-trp-based RRAM exhibited stable BRS characteristics, as shown in Figure 3b. To observe the BRS, a dual voltage sweep from +2.5 to −2.5 V was applied to the L-trp-based RRAM. A clear set process of switching from HRS to LRS was observed at a $V_{SET}$ of approximately 2.09 V in the positive bias region. In contrast, a reset process, switching from LRS to HRS, was observed at a $V_{RESET}$ of approximately −1.72 V in the negative bias region. The on/off ratio between HRS and LRS, measured at a read voltage ($V_{READ}$) of 0.1 V, was $1.94 \times 10^4$, confirming a high memory window.

Following the confirmation of stable BRS characteristics, the memory reliability of the L-trp-based RRAM was evaluated through data retention and endurance testing. Figure 3c shows the data retention test results for the HRS and LRS states at a $V_{READ}$ of 0.1 V for $10^5$ s. Even after $10^5$ s, both resistance states were stably maintained without any noticeable degradation, and the high on/off ratio was also preserved, demonstrating reliable memory characteristics. Additionally, consecutive switching cycles were performed to evaluate endurance. Figure 3d presents the *I–V* characteristics for 1000 cycles, which show highly consistent BRS characteristics. To demonstrate this more clearly, Figure 3e shows the HRS and LRS resistance values at $V_{READ}$ of 0.1 V for each cycle, confirming that the two states remain clearly distinguishable and that a stable on/off ratio is maintained throughout the repeated cycles.

Finally, Figure 3f shows the cumulative probability distributions of the $V_{SET}$ and $V_{RESET}$ values measured after 1000 cycles. The



16163028, 2026, 92, Downloaded from https://advanced.onlinelibrary.wiley.com/doi/10.1002/adfm.78971 by Yonsei University Library, Wiley Online Library on [22/11/2026]. See the Terms and Conditions (https://onlinelibrary.wiley.com/terms-and-conditions) on Wiley Online Library for rules of use; OA articles are governed by the applicable Creative Commons License

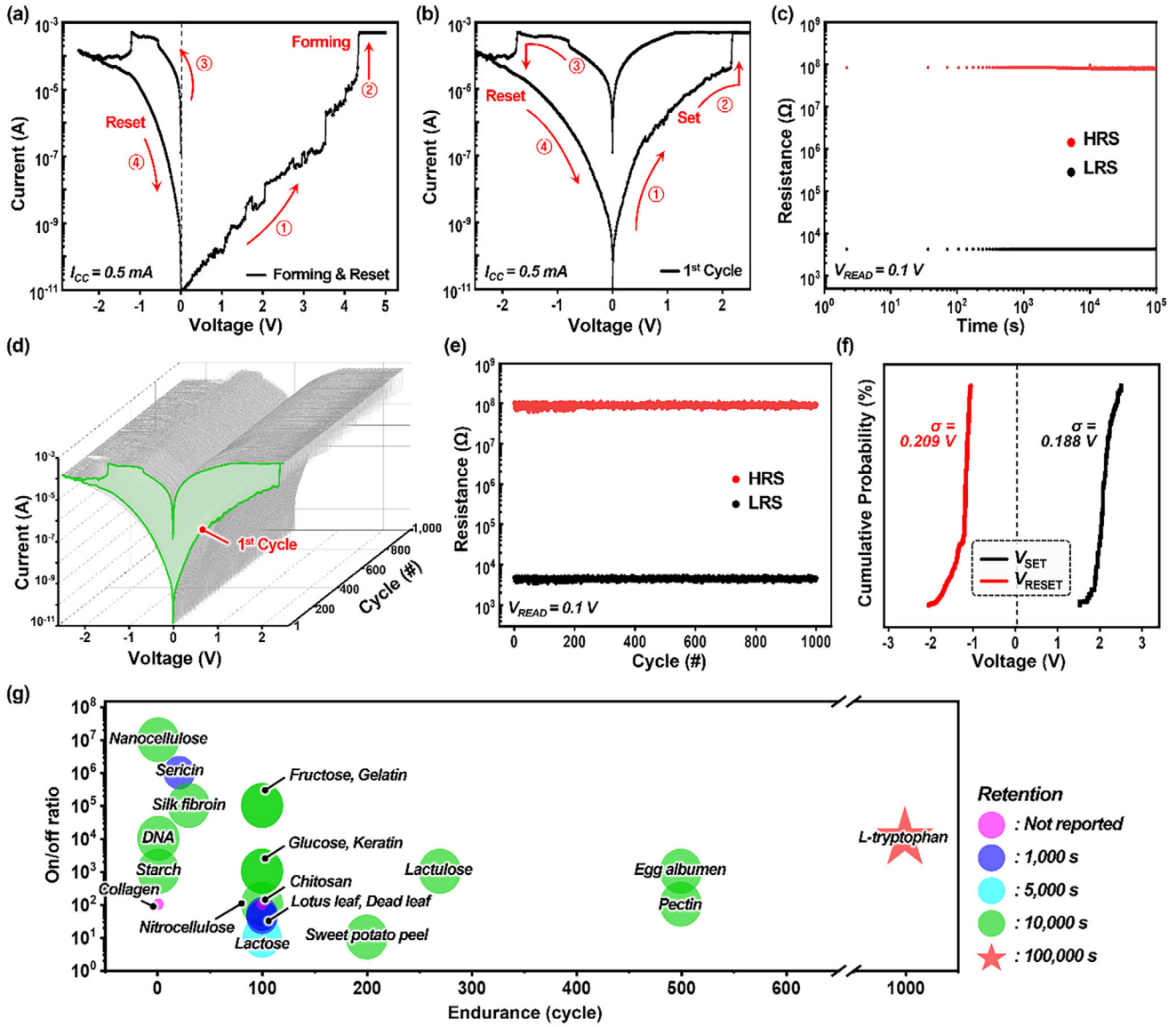



**FIGURE 3** | Electrical characteristics and reliability of the L-trp-based RRAM. (a) *I–V* characteristics of the initial forming and reset processes under a 0.5 mA of $I_{CC}$, (b) BRS *I–V* characteristics of the first cycle, and (c) data retention test results of the HRS and LRS for $10^5$ s of L-trp-based RRAM. (d) Endurance test results and (e) resistance distribution of HRS and LRS at $V_{READ}$ of 0.1 V and (f) cumulative probability distribution of $V_{SET}$ and $V_{RESET}$ during the endurance test of 1,000 cycles of L-trp-based RRAM. (g) Performance comparison of the L-trp-based RRAM with previously reported naturally sourced material-based RRAM in terms of on/off ratio, endurance, and retention. The bubble size and color represent the retention time as indicated in the legend.

fact that both the $V_{SET}$ and $V_{RESET}$ show a tight distribution, with standard deviations ($\sigma$) of 0.188 and 0.209 V, respectively, indicates that the cycle-to-cycle uniformity is stable, ensuring predictable switching operations. Collectively, the high on/off ratio of $1.94 \times 10^4$, stable data retention for $10^5$ s, endurance of over 1000 cycles, and stable $V_{SET}$ and $V_{RESET}$ uniformity are results that compare favorably with the performance of many previously reported naturally sourced material-based RRAM, as shown in Table 1. To further visualize this comparison, Figure 3g presents a bubble chart that simultaneously compares the on/off ratio, endurance, and retention of the L-trp-based RRAM against all previously reported naturally sourced material-based RRAM listed in Table 1. The bubble size and color represent the retention time. As clearly shown, the L-trp-based RRAM is positioned in the upper-right region of the chart, demonstrating a well-balanced combination of high on/off ratio (~$10^4$), endurance (1000 cycles), and long retention time ($10^5$ s) without any metal nanoparticle doping or inorganic hybrid synthesis. While individual metrics such as on/off ratio or retention time have been surpassed by certain other naturally sourced materials (e.g., cellulose achieves ~$10^7$ on/off ratio), these systems typically exhibit limited endurance or retention time. The L-trp-based RRAM achieves the most balanced performance across all three key metrics simultaneously, highlighting the advantage of the molecular-level design approach based on the intrinsic properties of L-trp.



16163028, 2026, 92, Downloaded from https://advanced.onlinelibrary.wiley.com/doi/10.1002/adfm.78971 by Yonsei University Library, Wiley Online Library on [22/11/2026]. See the Terms and Conditions (https://onlinelibrary.wiley.com/terms-and-conditions) on Wiley Online Library for rules of use; OA articles are governed by the applicable Creative Commons License

**TABLE 1** | Summary of the naturally sourced material-based RRAM with seven categories.

| Category | Switching layer | $V_{SET}$ (V) | $V_{RESET}$ (V) | On/off ratio | Endurance (Cycle) | Retention (s) | Refs. |
|---|---|---|---|---|---|---|---|
| Monosaccharides | Glucose | 3.46 | −1.84 | $10^3$ | 100 | $10^4$ | [16] |
| | Fructose | 2.40 | −1.61 | $10^5$ | 100 | $10^4$ | [17] |
| Disaccharides | Lactose | 1.20 | −0.60 | — | 100 | $5\times10^3$ | [18] |
| | Lactulose | 3.15 | −1.05 | $10^3$ | 270 | $10^4$ | [19] |
| Polysaccharides | Starch | 0.90 | — | $10^3$ | — | $10^4$ | [20] |
| | Nanocellulose | 1.00 | −0.50 | $10^7$ | — | $10^4$ | [21] |
| | Chitosan | 1.00 | −1.30 | $10^2$ | 100 | — | [22] |
| | Nitrocellulose | 2.65 | −1.67 | $10^2$ | 100 | $10^4$ | [23] |
| | Pectin | 1.00 | −0.50 | $10^2$ | 500 | $10^4$ | [24] |
| Protein | Collagen | — | — | $10^2$ | — | — | [25] |
| | Sericin | 2.50 | −0.80 | $10^6$ | 21 | $10^3$ | [26] |
| | Silk fibroin | 1.70 | −1.20 | $10^5$ | 30 | $10^4$ | [27] |
| | Keratin | — | — | $10^3$ | 100 | $10^4$ | [28] |
| | Gelatin | 0.90 | −1.35 | $10^5$ | 100 | $10^4$ | [29] |
| | Egg albumen | — | — | $10^3$ | 500 | $10^4$ | [30] |
| Nucleic acids | DNA[a)] | — | −2.00 | $10^4$ | — | $10^4$ | [31] |
| Plant-derived materials | Lotus leaf | 5.00 | −3.00 | 4×10 | 100 | $10^3$ | [32] |
| | Dead leaf | 1.00 | −1.50 | 5×10 | 100 | $10^3$ | [33] |
| | Sweet potato peel | — | — | — | 200 | $10^4$ | [34] |
| Amino acids | L-tryptophan | 2.09 | −1.72 | ~$10^4$ | 1,000 | $10^5$ | This work |

[a]Deoxyribo nucleic acid.

Based on the memory reliability confirmed at the device level, the retention characteristics of the 6 × 6 L-trp-based RRAM crossbar array were evaluated over $10^5$ s. Figure 4a shows a schematic of the fabricated 6×6 L-trp-based RRAM crossbar array. To visually demonstrate the retention characteristics of the array, a $V_{FORM}$ was selectively applied to specific points corresponding to the letters "L" and "T."

To evaluate the retention characteristics of the 6 × 6 L-trp-based RRAM crossbar array, a $V_{FORM}$ was first applied to the specific points corresponding to the "L" and "T" patterns to switch them to the LRS. As shown in Figure 4b, the current values at specific points were remeasured after $10^5$ s. Figure 4c displays a series of 3D bar plots showing the changes in current values for all points in the 6 × 6 L-trp-based RRAM crossbar array during this process. Before forming, all points were in the HRS. After creation, only the points in the "L" and "T" patterns are clearly switched to the LRS.

Quantitatively, the current at the points to which the $V_{FORM}$ was applied was measured at an $I_{CC}$ of 0.5 mA. After $10^5$ s, the current values of these specific points were stably maintained within a range from a minimum of $1.42 \times 10^{-3}$ A to a maximum of $3.14 \times 10^{-3}$ A. Figure S11 shows the detailed current values at each point after $10^5$ s. These results demonstrate that the 6 × 6 L-trp-based RRAM crossbar array has the potential to store and retain practical data reliably.

Following confirmation of the high memory reliability and data-storage capability of L-trp-based RRAM, we aimed to elucidate its fundamental carrier-conduction mechanism. This investigation focuses on charge transport within the L-trp active layer, distinct from the role of the $AlO_x$ interfacial layer filament.

In general, the conduction mechanism in the HRS of an organic-based RRAM is described by a space-charge-limited current (SCLC) conduction model. The SCLC conduction model is explained by Ohm's law, trap-filled-limited (TFL), and Mott–Gurney's law, as shown in Equations 1, 2, and 3, respectively.

$$J_{Ohm} = qn_0\mu\frac{V}{d} \propto V \tag{1}$$

$$J_{TFL} = \frac{9}{8}\mu\varepsilon q\frac{V^2}{d^3} \propto V^2 \tag{2}$$

$$J_{Mott} = \frac{9}{8}\mu\varepsilon\frac{V^2}{d^3} \propto V^2 \tag{3}$$

where $J$, $q$, $n_0$, $\mu$, $V$, $d$, and $\varepsilon$ are current density, electric charge, free carrier, mobility, applied voltage, dielectric thickness, and dielectric permittivity, respectively [61, 62]. In the low-voltage regime, immediately after the voltage is applied, the current flows



16163028, 2026, 92, Downloaded from https://advanced.onlinelibrary.wiley.com/doi/10.1002/adfm.78971 by Yonsei University Library, Wiley Online Library on [22/11/2026]. See the Terms and Conditions (https://onlinelibrary.wiley.com/terms-and-conditions) on Wiley Online Library for rules of use; OA articles are governed by the applicable Creative Commons License

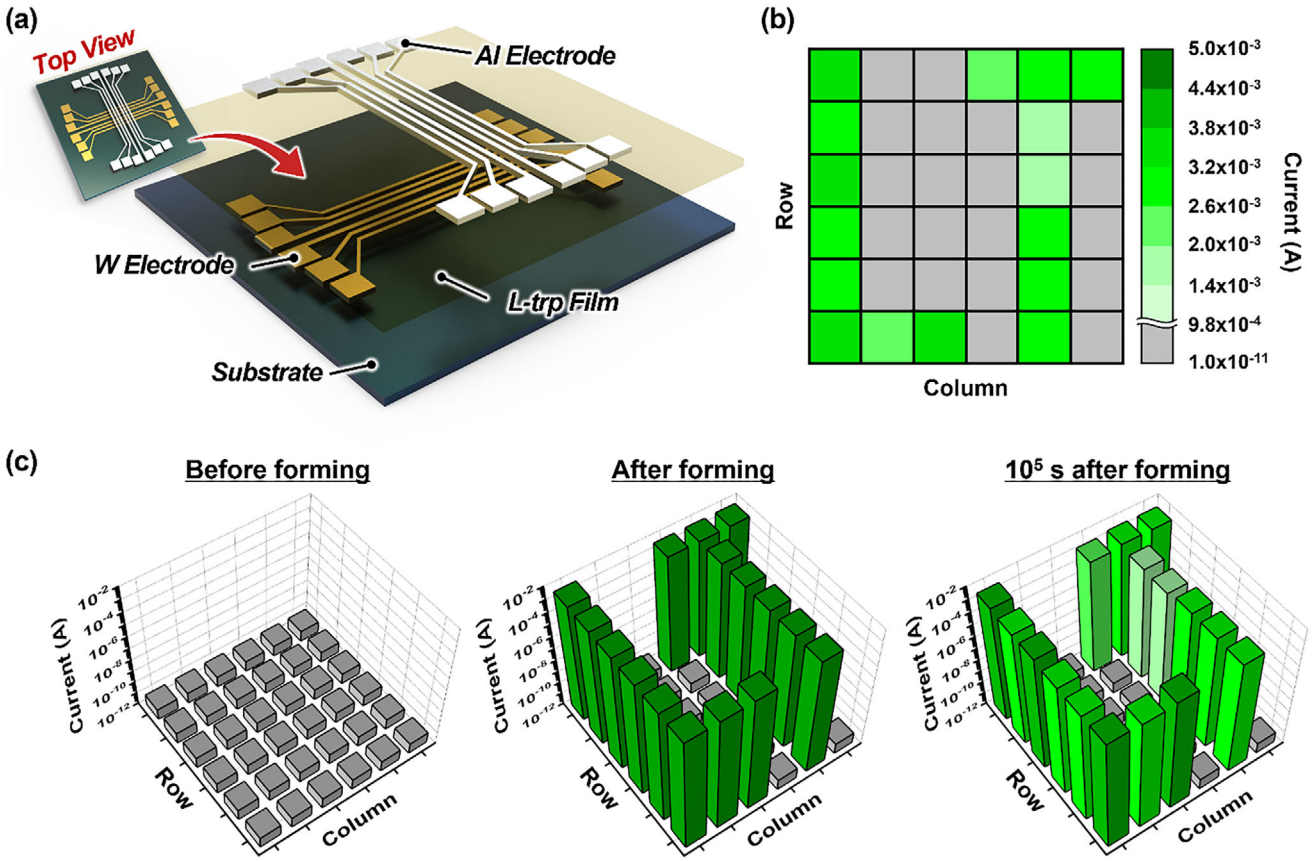



**FIGURE 4** | Retention characteristics in a 6 × 6 L-trp-based RRAM crossbar array. (a) Schematic diagram of the fabricated 6 × 6 L-trp-based RRAM crossbar array. (b) A current map showing the letters "L" and "T" by selectively switching to the LRS after a $10^5$ s retention test. (c) 3D bar plots of the current distribution across the array before forming, immediately after forming, and after a $10^5$ s retention test.

based on the free electrons existing within the organic active layer rather than the electrons injected from the top electrode. In this regime, the current flow is not significantly affected by the electrodes or traps within the organic active layer. This is known as Ohm's law and is characterized by a slope (S) of approximately 1 in the logarithmic *I*–*V* characteristic, as shown in Equation (1) [63]. When the voltage is increased beyond the regime dominated by Ohm's law, electrons injected from the top electrode begin to participate in the current flow. While these injected electrons fill the traps in the organic active layer, the electrons occupying the traps are simultaneously detrapped and move to the bottom electrode, thereby contributing to the current flow. In this regime, the current increases relatively steeply, known as TFL, and is characterized by an S value of approximately 2 in the logarithmic *I*–*V* characteristic, as shown in Equation (2). As the voltage is increased beyond the TFL regime, electrons injected from the top electrode fill all traps in the organic active layer, reaching a trap-free state. In this trap-free state, the concentration of electrons injected from the top electrode is sufficiently high, and trap-filling ceases. Consequently, electrons from the top electrode move to the bottom electrode, allowing current to flow. This is described by the Mott–Gurney law and is characterized by an S value of approximately 2 in the logarithmic *I*–*V* characteristic, as shown in Equation 3 [64].

To apply this SCLC model to the HRS conduction mechanism of the L-trp-based RRAM, the positive bias region of the *I*–*V* characteristics as shown in Figure 5a was replotted on a double logarithmic plot, as shown in Figure 5b. The HRS regions in the replotted *I*–*V* characteristics can be divided into three distinct linear sections. In the low-voltage "region A," the S value is 1.32, which is close to 1, indicating Ohm's law of conduction. As the voltage increases into "region B" and "region C," S values become 2.06 and 2.14, respectively. These S values are close to 2, indicating TFL and Mott–Gurney's law of conduction. Therefore, it is experimentally confirmed that charge transport in the HRS of the L-trp active layer follows the SCLC conduction model.

By combining this SCLC conduction model with the previously confirmed presence of $AlO_x$ interfacial layer, a comprehensive switching mechanism for the L-trp-based RRAM can be proposed, as illustrated in Figure 5c. When a strong positive voltage is applied to the L-trp-based RRAM in its initial insulating state, CFs that act as pathways for electrons are formed within the $AlO_x$ interfacial layer. Here, CFs are formed when a positive bias is applied, causing Al—O bonds within the $AlO_x$ interfacial layer to dissociate under the high electric field (~$10^9$ V/m), generating oxygen vacancies that create localized conductive pathways through the oxide layer [65–67]. As shown in Figure S12 and Table S3, this oxygen-vacancy-based filament mechanism is supported by the XPS analysis of the $AlO_x$ interfacial layer before and after the forming process, extracted at the same interfacial position under identical depth-profiling conditions. The Al—O bond proportion systematically decreases while the



16163028, 2026, 92, Downloaded from https://advanced.onlinelibrary.wiley.com/doi/10.1002/adfm.78971 by Yonsei University Library, Wiley Online Library on [22/11/2026]. See the Terms and Conditions (https://onlinelibrary.wiley.com/terms-and-conditions) on Wiley Online Library for rules of use; OA articles are governed by the applicable Creative Commons License

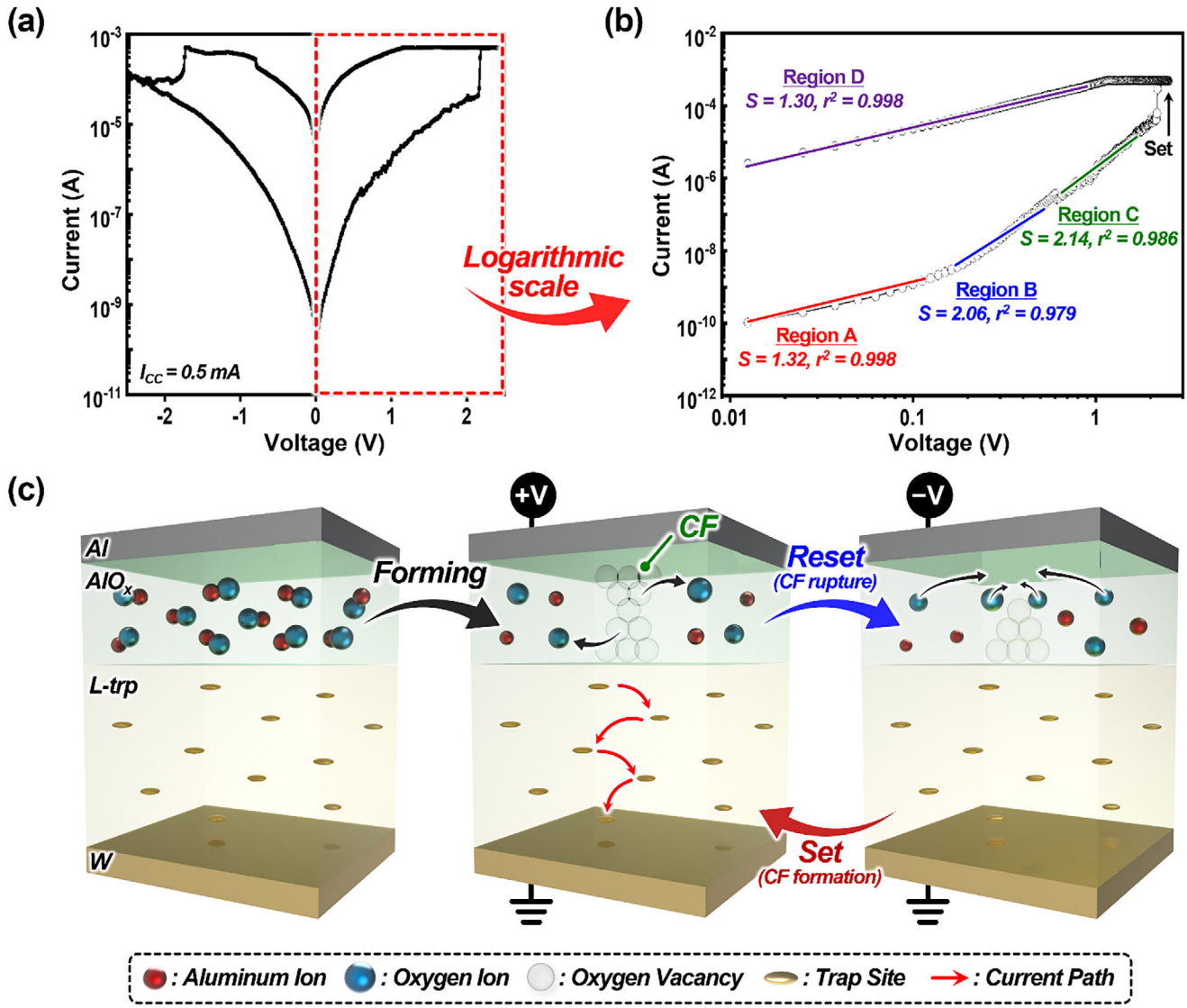



**FIGURE 5** | Conduction mechanism and switching model of the L-trp-based RRAM. (a) BRS *I–V* characteristics and (b) double logarithmic *I–V* characteristics for the positive voltage region of the L-trp-based RRAM. (c) Schematic illustration of the oxygen-vacancy-based switching mechanism, illustrating the forming, set, and reset processes within the $AlO_x$ interfacial layer of the L-trp-based RRAM.

Al–Al proportion increases after forming; since XPS averages over the entire probed area whereas the filaments occupy only a localized fraction of it, this area-averaged change reflects a pronounced Al–O dissociation within the localized filament regions. At this point, electrons migrate from the top electrode to the bottom electrode through the oxygen-vacancy-based CFs within the $AlO_x$ interfacial layer, and the trap sites are attributed to the indole rings within the L-trp active layer. This forming process switches the L-trp-based RRAM to the LRS, enabling it to be in a switchable state. Subsequently, when a negative bias is applied to the Al top electrode, the oxygen-vacancy-based CFs within the $AlO_x$ interfacial layer rupture as oxygen ions recombine with the vacancy sites, thereby restricting electron migration and switching the device back to the HRS via the reset process. When a positive bias is applied again to the Al top electrode, the oxygen vacancies are regenerated within the $AlO_x$ interfacial layer, reforming the CFs and switching the device back to the LRS via the set process. Through this set-and-reset cycle governed by oxygen vacancy generation and annihilation within the $AlO_x$ interfacial layer, the L-trp-based RRAM operates as a resistive-switching memory device. In the HRS, charge conduction proceeds through trap-mediated SCLC transport via the indole-ring trap sites in the L-trp active layer, as established earlier in this section.

To experimentally verify that the indole ring serves as the primary trap site, RRAM devices were fabricated using five different amino acids under identical processing conditions (Al/amino acid/W structure): L-glycine (L-gly, no aromatic side chain), L-histidine (L-his, imidazole ring), L-phenylalanine (L-phe, benzene ring), L-tyrosine (L-tyr, phenol ring), and L-trp (indole ring). All five amino acids share the same backbone structure ($NH_3^+$ and $COO^-$ groups) but differ exclusively in their side chains, thereby isolating the role of the aromatic ring system in resistive switching. As shown in Figure S13 and Table S4, the glycine-based RRAM exhibited no resistive switching behavior, showing anomalously high initial current due to the absence of aromatic trap sites that could capture and retain electrons;



16163028, 2026, 92, Downloaded from https://advanced.onlinelibrary.wiley.com/doi/10.1002/adfm.78971 by Yonsei University Library, Wiley Online Library on [22/11/2026]. See the Terms and Conditions (https://onlinelibrary.wiley.com/terms-and-conditions) on Wiley Online Library for rules of use; OA articles are governed by the applicable Creative Commons License

without trap sites, the active layer functions merely as a current-limiting series resistance. The L-his-, L-phe-, and L-tyr-based RRAMs all showed partial resistive switching, with the switching characteristics becoming progressively more pronounced in the order of L-his, L-phe, and L-tyr. This trend is attributed to their progressively increasing trap densities, as quantified below (Table S5). Nevertheless, all three devices exhibited less pronounced set and reset processes compared to L-trp, consistent with the shallower trap levels provided by their smaller $\pi$-systems (imidazole: 5-membered ring with 6 $\pi$-electrons; benzene and phenol: 6 $\pi$-electrons each). Among all five amino acids, the L-trp-based RRAM exhibited stable bipolar resistive switching with a well-defined on/off ratio, demonstrating that the indole ring—with its extended 10 $\pi$-electron conjugated system—provides the deepest and most effective trap levels among the standard amino acid side chains.

To further support this finding quantitatively, the trap density ($N_T$) was extracted from the SCLC fitting data using the trap-filled limit voltage ($V_{TFL}$):

$$N_T = 2\varepsilon_0\varepsilon_r V_{TFL}/qd^2 \quad (4)$$

where $\varepsilon_0$ is the vacuum permittivity, $\varepsilon_r$ is the relative permittivity, $V_{TFL}$ is the transition voltage from the Ohmic to the TFL regime, $q$ is the elementary charge, and $d$ is the active layer thickness [68]. In the organic RRAM literature, it is a widely accepted convention to use an assumed $\varepsilon_r$ value rather than direct measurement, with $\varepsilon_r \approx 3$ being the standard value for most organic semiconductors [69]. Additionally, solid-state amino acids in powder or crystal form exhibit similar dielectric constants in the range of $\varepsilon_r \approx 2$–4, regardless of the specific amino acid species [70]. Therefore, a uniform $\varepsilon_r = 3$ was applied to all five amino acid devices, ensuring that the comparison isolates the effect of the side chain exclusively. As summarized in Table S5, L-trp exhibited the highest trap density of $1.91 \times 10^{17}$ cm$^{-3}$, followed by L-tyr ($1.64 \times 10^{17}$ cm$^{-3}$), L-phe ($1.38 \times 10^{17}$ cm$^{-3}$), L-his ($1.10 \times 10^{17}$ cm$^{-3}$), and L-gly ($8.29 \times 10^{16}$ cm$^{-3}$). L-gly exhibited the lowest $V_{TFL}$ and correspondingly the lowest trap density, consistent with the absence of aromatic trap sites. This systematic trend—in which trap density increases with the extent of $\pi$-conjugated system in the aromatic side chain—provides compelling experimental evidence that the indole ring of L-trp serves as the primary charge trap site in the organic active layer.

Additionally, to confirm the influence of the $AlO_x$ interfacial layer on L-trp-based RRAM operation and to decouple the effect of electrode work function from interfacial oxide formation, control experiments were performed using three different top electrode configurations. Before discussing the experimental results, we note that the energy band alignment between the electrodes and the L-trp active layer does not govern the resistive switching mechanism in this system. As shown in Figure S14a, although the band offset ($\Phi_B$) between the top electrode work function ($\Phi_{TE}$) and the organic LUMO level creates an energy barrier at the metal/organic interface, a comprehensive review of bio-organic RRAM has established that carrier conduction in the HRS of all reported bio-organic-based RRAMs is universally governed by bulk-limited SCLC, regardless of the electrode material, polarity of biasing, or work function difference between the two electrodes [61]. In our device structure, the top electrode/LUMO $\Phi_B$ is expected to be > 1 eV based on the general trend observed across all bio-organic materials characterized to date ($\Phi_B \approx 2.0$–2.7 eV), which precludes thermionic electron injection. Moreover, the 5-nm-thick wide-bandgap $AlO_x$ interfacial layer ($E_G \approx 6.5$–8.7 eV) between the top electrode and the organic layer presents an even larger barrier to direct carrier injection, as shown in Figure S14b. Therefore, the switching mechanism proceeds through oxygen-vacancy-based conductive filament formation and rupture within the $AlO_x$ layer (filament region), combined with SCLC-governed charge transport through the L-trp active layer (SCLC region).

First, a Pt top electrode ($\Phi_{Pt} \approx 5.64$ eV), a noble metal that does not form an interfacial oxide with the L-trp active layer due to its highly positive standard electrode reduction potential of 1.18 V, was deposited. As expected, the Pt/L-trp/W device exhibited no resistive switching, as shown in Figure S15a. Second, to verify that this absence of switching is attributable to the lack of an interfacial oxide rather than the high work function of Pt, a Ni top electrode ($\Phi_{Ni} \approx 5.15$ eV) was employed. Ni has a work function much closer to Pt than to Al ($\Phi_{Al} \approx 4.13$ eV), yet possesses a standard electrode reduction potential of −0.26 V, enabling spontaneous $NiO_x$ formation at the Ni/L-trp interface—albeit less readily than Al of −1.66 V [71, 72]. As shown in Figure S15b, the Ni/L-trp/W device exhibited resistive switching characteristics, demonstrating that a high work function electrode does not preclude resistive switching when an interfacial oxide is present. The relatively less stable switching observed in the Ni-based device compared to the Al-based device is consistent with the higher standard electrode reduction potential of Ni, which results in a less well-developed $NiO_x$ interfacial layer. Third, to provide conclusive evidence, a thin 5-nm-thick $AlO_x$ layer (comparable to the thickness of the naturally formed $AlO_x$ in the Al-based device) was intentionally deposited between the Pt top electrode and the L-trp active layer by sputtering. Remarkably, the Pt/$AlO_x$/L-trp/W device exhibited clear bipolar resistive switching, as shown in Figure S15c, in stark contrast to the Pt/L-trp/W device without $AlO_x$. Since the only difference between these two Pt-based devices was the presence of the ~5 nm $AlO_x$ layer, this result unequivocally confirms that the $AlO_x$ interfacial layer—not the electrode work function—is the essential component for resistive switching. The combined results of the three control experiments (Pt, Ni, Pt with $AlO_x$) are summarized in Table S6.

To further examine how the interfacial oxide thickness governs the switching behavior, we fabricated Pt/$AlO_x$/L-trp/W devices in which the $AlO_x$ layer was intentionally deposited by sputtering at four thicknesses (3, 5, 10, and 15 nm), as shown in Figure S16. The switching behavior varies monotonically with the $AlO_x$ thickness: the 3 nm device shows metallic-like conduction without clear switching, the 5 nm device — matching the thickness of the naturally formed $AlO_x$ — exhibits stable bipolar resistive switching, whereas the 10 and 15 nm devices are too thick to undergo forming within the applied voltage range and remain in their initial insulating state. This confirms that ~5 nm, the thickness spontaneously produced by the self-limiting carboxylate reaction, corresponds to the optimal interfacial oxide thickness for resistive switching.

The multistate resistive switching behavior was systematically analyzed to evaluate the multistate potential of the L-trp-based RRAM. One of the most representative methods for



16163028, 2026, 92, Downloaded from https://advanced.onlinelibrary.wiley.com/doi/10.1002/adfm.78971 by Yonsei University Library, Wiley Online Library on [22/11/2026]. See the Terms and Conditions (https://onlinelibrary.wiley.com/terms-and-conditions) on Wiley Online Library for rules of use; OA articles are governed by the applicable Creative Commons License

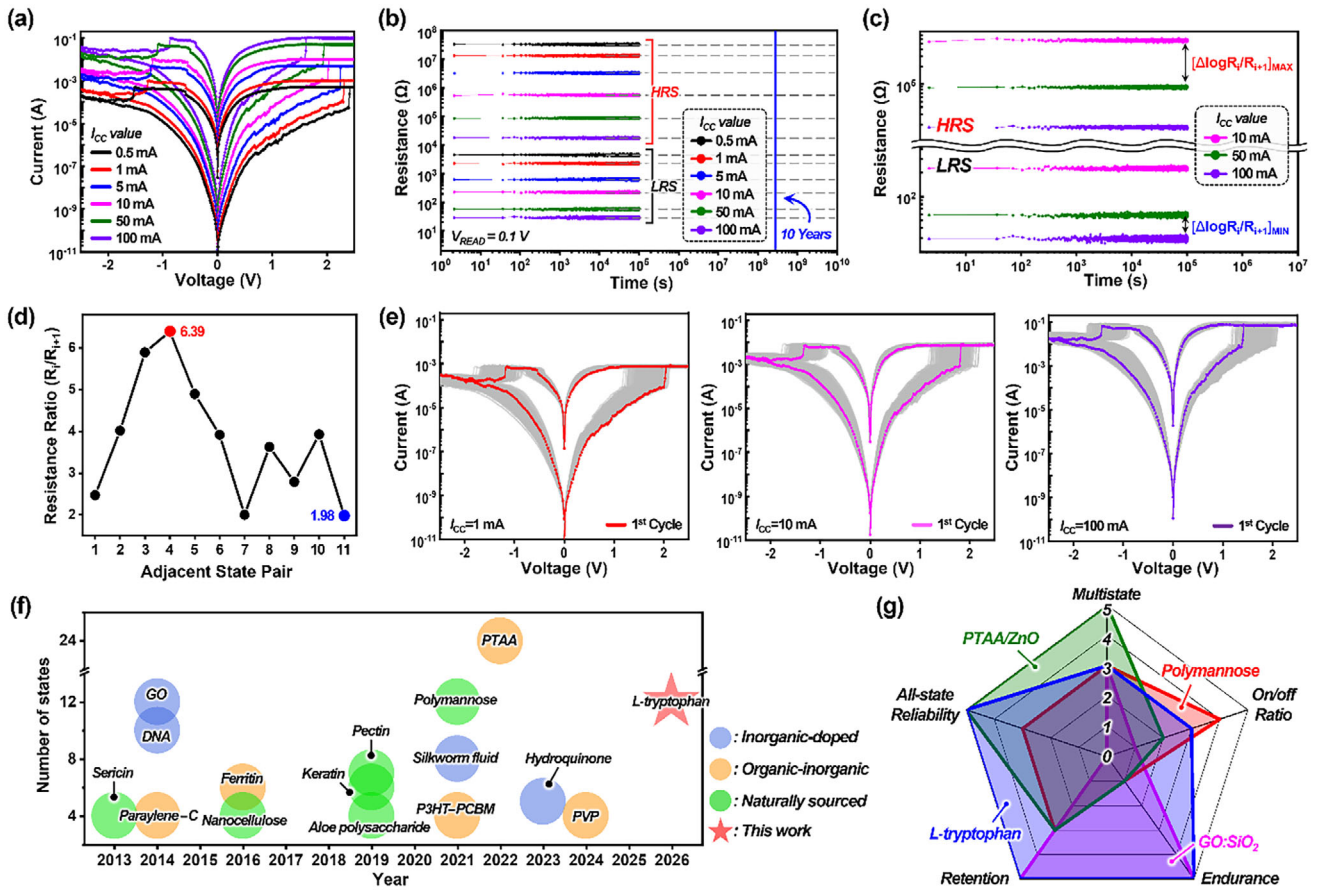



**FIGURE 6** | Multistate resistive switching characteristics and benchmarking of the L-trp-based RRAM. (a) *I–V* characteristics obtained by varying the $I_{CC}$ from 0.5 to 100 mA and (b) retention characteristics for $10^5$ s of the 12 resistance states. (c) A magnified view of the retention characteristics with the maximum and minimum state differences and (d) resistance ratio between adjacent resistance states. (e) Endurance characteristics over 1000 switching cycles at representative $I_{CC}$ conditions of 1, 10, and 100 mA. (f) Bubble chart comparing the number of multistate levels achieved by organic RRAM via $I_{CC}$ modulation, classified into three categories: inorganic-doped, organic–inorganic hybrid, and naturally sourced materials and (g) radar chart comparing the L-trp-based RRAM against GO:$SiO_2$-, PTAA/ZnO-, and polymannose-based RRAMs across five key metrics.

implementing multistate RRAM is to modulate the $I_{CC}$ during the set process, which dictates the formation of CFs [73]. The $I_{CC}$ modulates the robustness of CFs. A larger $I_{CC}$ induces thicker, stronger CFs, resulting in an LRS with a higher current. By contrast, a smaller $I_{CC}$ forms thinner, weaker CFs, resulting in an LRS with a lower current [74].

Figure 6a shows the *I–V* characteristics measured by sequentially increasing the $I_{CC}$ to 0.5, 1, 5, 10, 50, and 100 mA to confirm multistate resistive switching behavior, and Figure S17 shows the $V_{SET}$ and $V_{RESET}$ for each $I_{CC}$ condition. As expected, with increasing $I_{CC}$, the current LRS level gradually increases, and the HRS level rises accordingly. Furthermore, as the $I_{CC}$ increases, $V_{SET}$ decreases owing to the formation of stronger filaments, and $V_{RESET}$ consequently tends to increase to rupture the stronger filament. Thus, six pairs of LRS/HRS states, that is, 12 resistance states, are obtained. To verify the stability of each resistance state, the retention characteristics of all 12 resistance states were evaluated for $10^5$ s, as shown in Figure 6b. All 12 resistance states, measured at a $V_{READ}$ of 0.1 V, were stably maintained for $10^5$ s without noticeable degradation, demonstrating high non-volatile multistate characteristics. Each of the 12 resistance states was extrapolated to remain stable for approximately 10 years.

For reliable multistate memory characteristics, each state must be clearly distinguishable from the others, with no overlap. For the quantitative analysis, 12 resistance states were sorted from the highest resistance ($R_1$: HRS @ 0.5 mA) to the lowest resistance ($R_{12}$: LRS @ 100 mA). Figure 6c shows a magnified view of the retention characteristics with the maximum and minimum state differences, and Figure 6d shows the adjacent resistance state ratio ($R_i/R_{i+1}$). The analysis revealed a maximum resistance ratio of 6.39 between $R_4$ (HRS @ 10 mA) and $R_5$ (HRS @ 50 mA), and a minimum resistance ratio of 1.98 between $R_{11}$ (LRS @ 50 mA) and $R_{12}$ (LRS @ 100 mA). A minimum resistance ratio of 1.98 indicates that all 12 resistance states differ by at least 2 times from their adjacent states.

To validate the cycling reproducibility of all 12 resistance states, endurance testing was performed at five $I_{CC}$ conditions with 1, 5, 10, 50, and 100 mA over 1000 switching cycles. Figure 6e presents the *I–V* endurance characteristics at $I_{CC}$ = 1, 10, and 100 mA, where the first cycle is highlighted in color and subsequent cycles are shown in gray, while the endurance data at $I_{CC}$ = 5 and 50 mA are provided in Figure S18. In all conditions, the switching voltages and current levels at both HRS and LRS remained tightly distributed over 1000 cycles, confirming the cyclic reproducibility of the multistate operation. The resistance values of all HRS



16163028, 2026, 92, Downloaded from https://advanced.onlinelibrary.wiley.com/doi/10.1002/adfm.78971 by Yonsei University Library, Wiley Online Library on [22/11/2026]. See the Terms and Conditions (https://onlinelibrary.wiley.com/terms-and-conditions) on Wiley Online Library for rules of use; OA articles are governed by the applicable Creative Commons License

**TABLE 2** | Summary of the organic RRAM with multistate characteristics via $I_{CC}$ modulation, classified into three categories.

| Category | Switching layer | States | $I_{CC}$ range (A) | All-state reliability | Refs. |
|---|---|---|---|---|---|
| Inorganic-doped organic material | Hydroquinone:Zn | 5 | 0.5–5 m | Endurance(30), retention($10^3$) | [75] |
| | Silkworm fluid:Au | 8 | 0.06–20 m | Endurance only(70) | [76] |
| | DNA:Ni | 10 | 0.1–0.4 n | Not reported | [77] |
| | GO:$SiO_2$[a)] | 12 | 0.01–20 m | Not reported | [78] |
| Organic–inorganic hybrid material | PVP/$MoSe_2$[b)] | 4 | 0.1 m–1 m | Endurance(1,150), retention($10^4$) | [79] |
| | P3HT–PCBM/ZnO[c)] | 4 | 100–800 µ | Not reported | [80] |
| | Parylene-C/$HfO_x$ | 4 | 0.05–1 m | Retention only($10^4$) | [81] |
| | Ferritin/$FeO_x$ | 6 | 0.1–100 µ | Not reported | [82] |
| | PTAA/ZnO[d)] | 24 | 0.01–5 µ | Endurance(150), retention($10^3$) | [83] |
| Naturally sourced material | Sericin | 4 | 0.1–10 m | Endurance(21), retention($10^3$) | [26] |
| | Nanocellulose | 4 | 0.05–1 m | Retention only($10^3$) | [21] |
| | Pectin | 4 | 0.5–5 m | Endurance(150), retention($10^4$) | [24] |
| | Keratin | 6 | 1 m–5 m | Retention only($10^2$) | [29] |
| | Aloe polysaccharide | 7 | 0.1 µ–10 m | Not reported | [84] |
| | Polymannose | 12 | 0.1 µ–10 m | Retention only($10^4$) | [85] |
| | L-tryptophan | 12 | 0.5 m–100 m | Endurance(1,000), retention($10^5$) | This work |

[a]Graphene oxide;
[b]Poly(4-vinylphenol);
[c]poly(3-hexylthiophene)–phenyl-C61-butyric acid methyl ester;
[d]poly[bis(4-phenyl)(2,4,6-trimethylphenyl)amine].

and LRS levels over 1000 cycles are summarized in Figure S19, which demonstrates that all 12 resistance states were maintained without significant degradation. While a minor overlap between some adjacent states was observed in a small fraction of cycles, the overall state separation was preserved throughout the endurance test.

To systematically benchmark the multistate capability, Table 2 compares multistate organic RRAM studies achieved by modulating the $I_{CC}$, classified into three categories: inorganic-doped organic materials, organic–inorganic hybrid materials, and naturally sourced materials [21, 24, 26, 29, 75–85]. The bubble chart in Figure 6f visualizes the progression of multistate organic RRAM research achieved by modulating the $I_{CC}$ over time across the three categories. While the highest reported state count (24) was achieved by a PTAA/ZnO organic–inorganic hybrid structure utilizing an additional ZnO layer, the L-trp-based RRAM achieves 12 states using a pure naturally sourced material—matching the maximum for single naturally sourced materials. Figure 6g presents a radar chart comparing the L-trp-based RRAM against the highest-state device from each category—GO:$SiO_2$, PTAA/ZnO, and polymannose—across five key metrics: multistate, on/off ratio, endurance, retention, and all-state reliability. The normalization details are provided in Table S7. Although certain individual metrics such as on/off ratio (~$10^4$) or number of states (12) may appear moderate in the radar chart, an on/off ratio of ~$10^4$ already exceeds the threshold for reliable memory operation, and the 12 states represent the highest among pure naturally sourced materials. Notably, the L-trp-based RRAM exhibits a performance profile comparable to those of devices incorporating inorganic dopants or hybrid layers, despite being composed entirely of a pure naturally sourced material. Within the naturally sourced material category, the L-trp-based RRAM achieves the highest overall balanced performance, attaining the maximum scores on the endurance, retention, and all-state reliability axes simultaneously. This demonstrates that the molecular-level design approach based on the intrinsic properties of L-trp can achieve a level of multistate performance previously attainable only through inorganic doping or hybrid architectures.

For practical implementation of multistate RRAM in crossbar array architectures, several array-level challenges must be considered. First, sneak path currents through unselected cells can cause read errors in passive crossbar arrays, particularly when the selected cell is in the HRS. This universal challenge can be addressed by integrating a selector device in a one-selector-one-resistor (1S1R) configuration, which is expected to be compatible with the simple MIM structure and low operating voltage (~2 V) of the L-trp-based RRAM. Second, read disturbance is minimized by the large voltage margin (>1.4 V) between $V_{READ}$ (0.1 V) and the minimum $V_{SET}$ (~1.5 V), as confirmed by the stable retention of all 12 states for $10^5$ s at $V_{READ}$ = 0.1 V (Figure 6b). Third, write disturbance on unselected cells can be mitigated by the tight $V_{SET}$ and $V_{RESET}$ distributions ($\sigma$ = 0.188 V and 0.209 V, respectively; Figure 3f), which provide sufficient voltage margin for half-voltage or one-third-voltage biasing schemes. The exploration of 1S1R integration and large-scale array demonstration will be pursued in future work.

While the L-trp-based RRAM demonstrates competitive multistate performance—including 12 distinguishable resistance



16163028, 2026, 92, Downloaded from https://advanced.onlinelibrary.wiley.com/doi/10.1002/adfm.78971 by Yonsei University Library, Wiley Online Library on [22/11/2026]. See the Terms and Conditions (https://onlinelibrary.wiley.com/terms-and-conditions) on Wiley Online Library for rules of use; OA articles are governed by the applicable Creative Commons License

states, an on/off ratio of ~$10^4$, retention of $10^5$ s, and all-state cycling endurance and retention verification that is unmatched among naturally sourced material-based RRAM—the current endurance of 1000 DC switching cycles remains a limitation that warrants discussion. In Figure S20, beyond 1000 cycles, a stuck-at-LRS failure was observed, in which the set process remained functional but the reset process was no longer clearly defined. This degradation is attributed to the combined effect of two mechanisms: (i) progressive accumulation of oxygen vacancies within the $AlO_x$ interfacial layer under repeated electrical stress, which creates excessively robust conductive filaments that can no longer be ruptured under the applied reset voltage, and (ii) irreversible saturation of the indole ring trap sites within the L-trp active layer, where accumulated trapped charges transition the conduction from a reversible trap-filled-limited regime to a permanent trap-charge-limited current regime, progressively reducing the HRS resistance until the switching window collapses. To extend the endurance beyond 1000 cycles in future work, several complementary strategies targeting each degradation mechanism can be considered: (i) pulse-mode (AC) operation to reduce the energy dissipated per switching cycle and mitigate cumulative filament over-growth, which has been demonstrated to improve endurance by 3–4 orders of magnitude, (ii) controlled deposition of the $AlO_x$ interfacial layer via atomic layer deposition (ALD) to achieve more uniform and reproducible filament formation/rupture dynamics, suppressing the progressive accumulation of residual oxygen vacancies, and (iii) introduction of a 2D thermal management interlayer such as hexagonal boron nitride (h-BN) to dissipate Joule heat generated during the reset process and protect the thermally sensitive organic active layer from cumulative thermal degradation [86–88]. In our subsequent studies, we will systematically explore these strategies—individually and in combination—to push the endurance limit of the L-trp-based RRAM toward practically viable levels while preserving its advantageous multistate capability and naturally sourced material identity.

## 3 | Conclusions

In this study, L-trp-based RRAM was successfully fabricated, and its characteristics were systematically analyzed using the essential amino acid L-trp as a naturally sourced active layer. The presence of highly reactive carboxylate ions within the L-trp active layer was confirmed by FT-IR analysis. TEM, EDS mapping, and XPS analyses revealed that an $AlO_x$ interfacial layer was formed at the Al/L-trp interface owing to the interaction between the highly reactive carboxylate ions and the Al top electrode. The fabricated L-trp-based RRAM exhibited a high on/off ratio of $1.94 \times 10^4$, stable retention characteristics for $10^5$ s, and endurance of over 1000 cycles. Furthermore, array retention characteristics were demonstrated by successfully storing 'L' and 'T' patterns in a 6 × 6 L-trp-based RRAM crossbar array, with the current maintained for $10^5$ s. Moreover, multistate characteristics were achieved by establishing 12 distinct resistance states via $I_{CC}$ modulation. These results strongly suggest that L-trp is a promising, naturally sourced material for next-generation high-density memory devices.

## 4 | Experimental Section

### 4.1 | Preparation of L-trp Solution

L-trp solutions with concentrations of 1, 2, and 3 wt.% in DI water and 1, 2, 3, and 4 wt.% in DMSO were prepared by dissolving L-trp powder (Sigma-Aldrich, USA) in the corresponding solvents. The prepared solutions were stirred overnight and then aged for 24 h.

### 4.2 | Fabrication of the 6 × 6 L-trp-Based RRAM Crossbar Array

Initially, a heavily doped $p^+$-Si wafer substrate with thermally grown $SiO_2$ was sequentially cleaned with acetone, methanol, and DI water to remove surface contaminants. The W bottom electrode was deposited onto a cleaned substrate via radio frequency magnetron sputtering at 60 W for 30 min, using a shadow mask to pattern the crossbar array. Then, the prepared L-trp solution was filtered through a 0.2 μm polytetrafluoroethylene syringe filter and spin-coated onto the patterned W bottom electrode substrate at 3000 rpm for 30 s. Following deposition, the 20-nm-thick L-trp active layer was annealed on a hot plate at 85°C for 1 h. Finally, the Al top electrode was deposited via e-beam evaporator, using a shadow mask designed to complete the 6 × 6 L-trp-based RRAM crossbar array. Each memory cell of the 6 × 6 crossbar array was defined at the junction between the 140-μm-wide Al top electrode and the 157-μm-wide W bottom electrode, corresponding to a cell area of ~140 × 157 $\mu m^2$.

### 4.3 | Electrical Measurements

The electrical characteristics of the L-trp-based RRAM crossbar array were measured in the dark using a semiconductor parameter analyzer (Model 4200A; Keithley Instruments, USA).

### 4.4 | Device Characterization

The indole and carboxyl groups of the L-trp powder and film were identified using FT-IR spectroscopy (INVENIO, BRUKER, USA) in ATR mode with a diamond crystal under identical conditions (4000–400 $cm^{-1}$, 4 $cm^{-1}$ resolution). The surface topography and roughness of the L-trp film were characterized using atomic force microscopy (NX-10, Park Systems, Republic of Korea). The thickness of the L-trp layer was measured using a spectroscopic ellipsometer (Alpha-SE; J. A. Woollam, USA). The L-trp-based RRAM was imaged using TEM (Talos F200X, Thermo Fisher Scientific, USA; JEM-ARM200F NEOARM, JEOL, Japan), both equipped with EDS mapping. The layer composition of the L-trp-based RRAM was investigated using XPS depth profiling (K-alpha; Thermo Fisher Scientific, USA). The photograph of the fabricated device was taken with a digital camera, and the images of the crossbar array and individual memory cells were obtained using a digital microscope (VHX-7000, Keyence, Japan).



16163028, 2026, 92, Downloaded from https://advanced.onlinelibrary.wiley.com/doi/10.1002/adfm.78971 by Yonsei University Library, Wiley Online Library on [22/11/2026]. See the Terms and Conditions (https://onlinelibrary.wiley.com/terms-and-conditions) on Wiley Online Library for rules of use; OA articles are governed by the applicable Creative Commons License

### Author Contributions

**Moon Ho Lee**: writing – original draft, visualization, formal analysis, conceptualization, data curation. **Beom Soo Kim**: writing – review and editing, data curation, investigation. **Kunho Moon**: writing –review and editing, investigation, data curation. **Jong Bin An**: writing – review and editing. **Seok Gyu Hong**: writing – review and editing. **Sun Min Song**: writing – review and editing. **Hye Jin Son**: writing – review and editing. **Jae Seong Han**: writing – review and editing. **Hyun Jae Kim**: supervision, funding acquisition.


### Acknowledgements

This work was supported by the Technology Innovation Program (RS-2025-25454815) funded by the Ministry of Trade Industry & Energy (MOTIE, Korea).


### Conflicts of Interest

The authors declare no conflicts of interest.

### Data Availability Statement

The data that support the findings of this study are available on request from the corresponding author. The data are not publicly available due to privacy or ethical restrictions.

### References


1. Y. LeCun, Y. Bengio, and G. Hinton, "Deep Learning," *Nature* 521 (2015): 436–444, https://doi.org/10.1038/nature14539.

2. Z. Yang, S. Huo, Z. Zhang, et al., "High-Precision Multibit Opto-Electronic Synapses Based on $ReS_2$/h-BN/Graphene Heterostructure for Energy-Efficient and High-Accuracy Neuromorphic Computing," *Advanced Functional Materials* 35 (2025): 2509119, https://doi.org/10.1002/adfm.202509119.

3. R. Schmitt, M. Kubicek, E. Sediva, et al., "Accelerated Ionic Motion in Amorphous Memristor Oxides for Nonvolatile Memories and Neuromorphic Computing," *Advanced Functional Materials* 29 (2019): 1804782, https://doi.org/10.1002/adfm.201804782.

4. S.-M. Lee, W.-J. Lee, J.-Y. Bae, et al., "Ecofriendly Transfer Printing for Biodegradable Electronics Using Adhesion Controllable Self-Assembled Monolayers," *Advanced Functional Materials* 34 (2024): 2310612, https://doi.org/10.1002/adfm.202310612.

5. S. Yu, "Neuro-Inspired Computing With Emerging Nonvolatile Memorys," *Proceedings of the IEEE* 106 (2018): 260–285, https://doi.org/10.1109/JPROC.2018.2790840.

6. M. M. Waldrop, "The Chips are Down for Moore's Law," *Nature* 530 (2016): 144–147, https://doi.org/10.1038/530144a.

7. W. Qin, B. H. Kang, J. B. An, and H. J. Kim, "Indium Oxide Nanomesh-Based Electrolyte-Gated Synaptic Transistors," *Journal of Information Display* 22 (2021): 179–185, https://doi.org/10.1080/15980316.2021.1911866.

8. H. S. P. Wong, H. Y. Lee, S. Yu, et al., "Metal–Oxide RRAM," *Proceedings of the IEEE* 100 (2012): 1951–1970, https://doi.org/10.1109/JPROC.2012.2190369.

9. K. Xie, X. Li, and T. Cao, "Theory and Ab Initio Calculation of Optically Excited States—Recent Advances in 2D Materials," *Advanced Materials* 33 (2021): 1904306, https://doi.org/10.1002/adma.201904306.

10. G. U. Kamble, A. P. Patil, R. K. Kamat, J. H. Kim, and T. D. Dongale, "Promising Materials and Synthesis Methods for Resistive Switching Memory Devices: A Status Review," *ACS Applied Electronic Materials* 5 (2023): 2454–2481, https://doi.org/10.1021/acsaelm.3c00062.

11. X. Xing, M. Chen, Y. Gong, Z. Lv, S. T. Han, and Y. Zhou, "Building Memory Devices From Biocomposite Electronic Materials," *Science and Technology of Advanced Materials* 21 (2020): 100–121, https://doi.org/10.1080/14686996.2020.1725395.

12. S. Sandhu, A. Zumeit, Z. Tian, V. Vinciguerra, and R. Dahiya, "Semiconductor Manufacturing Wastewater Challenges and the Potential Solutions via Printed Electronics," *Iscience* 28 (2025): 113576, https://doi.org/10.1016/j.isci.2025.113576.

13. T. Y. Wang, W. C. Lai, Q. J. Xie, S. P. Chang, C. H. Kuo, and J. K. Sheu, "Thermally Oxidized $Al_xGa_{2-x}O_3$/n-$Al_{0.6}Ga_{0.4}$N:Si Unipolar Resistive Random-Access Memory," *ACS Applied Electronic Materials* 6 (2024): 3688–3694, https://doi.org/10.1021/acsaelm.4c00365.

14. K. S. Li, M. K. Huang, Y. H. Wang, Y. C. Tseng, and C. J. Su, "Wafer-Scale Fabrication of Al/$MoS_2$/Poly-Si Memristors and Insight of Mechanism on the Resistive Switching," *ACS Applied Electronic Materials* 6 (2024): 777–784, https://doi.org/10.1021/acsaelm.3c01314.

15. J. Xu, X. Zhao, X. Zhao, et al., "Memristors With Biomaterials for Biorealistic Neuromorphic Applications," *Small Science* 2 (2022): 2200028, https://doi.org/10.1002/smsc.202200028.

16. S. P. Park, Y. J. Tak, H. J. Kim, J. H. Lee, H. Yoo, and H. J. Kim, "Analysis of the Bipolar Resistive Switching Behavior of a Biocompatible Glucose Film for Resistive Random Access Memory," *Advanced Materials* 30 (2018): 1800722, https://doi.org/10.1002/adma.201800722.

17. Y. Xing, B. Sueoka, K. Y. Cheong, and F. Zhao, "Nonvolatile Resistive Switching Memory Based on Monosaccharide Fructose Film," *Applied Physics Letters* 119 (2021): 163302, https://doi.org/10.1063/5.0067453.

18. Y. Guo, W. Hu, F. Zeng, C. Zhang, Y. Peng, and Y. Guo, "Ultrafast Degradable Resistive Switching Memory Based on $\alpha$-lactose Thin Films," *Organic Electronics* 83 (2020): 105750, https://doi.org/10.1016/j.orgel.2020.105750.

19. B. S. Kim, J. B. An, D. H. Choi, et al., "Biocompatible Lactulose-Based Resistive Random Access Memory for Implantable Electronics," *ACS Applied Materials & Interfaces* 17 (2025): 34317–34326, https://doi.org/10.1021/acsami.5c04446.

20. N. Raeis-Hosseini and J. S. Lee, "Controlling the Resistive Switching Behavior in Starch-Based Flexible Biomemristors," *ACS Applied Materials & Interfaces* 8 (2016): 7326–7332, https://doi.org/10.1021/acsami.6b01559.

21. U. Celano, K. Nagashima, H. Koga, et al., "All-Nanocellulose Nonvolatile Resistive Memory," *NPG Asia Materials* 8 (2016): 310, https://doi.org/10.1038/am.2016.144.

22. K. M. Tran, D. P. Do, K. H. Ta Thi, and N. K. Pham, "Influence of Top Electrode on Resistive Switching Effect of Chitosan Thin Films," *Journal of Materials Research* 34 (2019): 3899–3906, https://doi.org/10.1557/jmr.2019.353.

23. J. H. Lee, S. P. Park, K. Park, and H. J. Kim, "Flexible and Waterproof Resistive Random-Access Memory Based on Nitrocellulose for Skin-Attachable Wearable Devices," *Advanced Functional Materials* 30 (2020): 1907437, https://doi.org/10.1002/adfm.201907437.

24. J. Xu, X. Zhao, Z. Wang, et al., "Biodegradable Natural Pectin-Based Flexible Multilevel Resistive Switching Memory for Transient Electronics," *Small* 15 (2019): 1803970, https://doi.org/10.1002/smll.201803970.

25. H. Wang, B. Zhu, H. Wang, X. Ma, Y. Hao, and X. Chen, "Ultra-Lightweight Resistive Switching Memory Devices Based on Silk Fibroin," *Small* 12 (2016): 3360–3365, https://doi.org/10.1002/smll.201600893.

26. H. Wang, F. Meng, Y. Cai, et al., "Sericin for Resistance Switching Device With Multilevel Nonvolatile Memory," *Advanced Materials* 25 (2013): 5498–5503, https://doi.org/10.1002/adma.201301983.

27. H. J. Liu, Z. C. Chen, Y. Y. Liang, and Y. C. Chang, "Design of Biodegradable Gelatin Resistive Memory With Remarkable Performance," *Organic Electronics* 125 (2024): 106979, https://doi.org/10.1016/j.orgel.2023.106979.

28. Y. C. Chen, H. C. Yu, C. Y. Huang, W. L. Chung, S. L. Wu, and Y. K. Su, "Nonvolatile Bio-Memristor Fabricated With Egg Albumen Film," *Scientific Reports* 5 (2015): 10022, https://doi.org/10.1038/srep10022.





16163028, 2026, 92, Downloaded from https://advanced.onlinelibrary.wiley.com/doi/10.1002/adfm.78971 by Yonsei University Library, Wiley Online Library on [22/11/2026]. See the Terms and Conditions (https://onlinelibrary.wiley.com/terms-and-conditions) on Wiley Online Library for rules of use; OA articles are governed by the applicable Creative Commons License

29. Q. Lin, S. Hao, W. Hu, et al., "Human Hair Keratin for Physically Transient Resistive Switching Memory Devices," *Journal of Materials Chemistry C* 7 (2019): 3315–3321, https://doi.org/10.1039/c8tc05334k.

30. Y. Zeng, B. Sun, H. Y. Yu, et al., "A Sustainable Biomemristive Memory Device Based on Natural Collagen," *Materials Today Chemistry* 13 (2019): 18–24, https://doi.org/10.1016/j.mtchem.2019.04.008.

31. J. Y. Lam, G. W. Jang, C. J. Huang, S. H. Tung, and W. C. Chen, "Environmentally Friendly Resistive Switching Memory Devices With DNA as the Active Layer and Bio-Based Polyethylene Furanoate as the Substrate," *ACS Sustainable Chemistry & Engineering* 8 (2020): 5100–5106, https://doi.org/10.1021/acssuschemeng.9b07168.

32. Y. Qi, B. Sun, G. Fu, et al., "A Nonvolatile Organic Resistive Switching Memory Based on Lotus Leaves," *Chemical Physics* 516 (2019): 168–174, https://doi.org/10.1016/j.chemphys.2018.09.008.

33. B. Sun, S. Zhu, S. Mao, et al., "From Dead Leaves to Sustainable Organic Resistive Switching Memory," *Journal of Colloid and Interface Science* 513 (2018): 774–778, https://doi.org/10.1016/j.jcis.2017.12.007.

34. S. Zhu, G. Zhou, W. Yuan, et al., "Non-Zero-Crossing Current-Voltage Hysteresis Behavior Induced by Capacitive Effects in Bio-Memristor," *Journal of Colloid and Interface Science* 560 (2020): 565–571, https://doi.org/10.1016/j.jcis.2019.10.087.

35. Y. Li, Q. Qian, X. Zhu, et al., "Recent Advances in Organic-Based Materials for Resistive Memory Applications," *InfoMat* 2 (2020): 995–1033, https://doi.org/10.1002/inf2.12120.

36. M. M. Rehman, H. M. M. ur Rehman, W. Y. Kim, et al., "Biomaterial-Based Nonvolatile Resistive Memory Devices Toward Ecofriendliness and Biocompatibility," *ACS Applied Electronic Materials* 3 (2021): 2832–2861, https://doi.org/10.1021/acsaelm.1c00078.

37. S. Du, Y. Song, J. Yuan, et al., "An Artificial Universal Tactile Nociceptor Based on 2D Polymer Film Memristor Arrays With Tunable Resistance Switching Behaviors," *ACS Applied Materials & Interfaces* 16 (2024): 33907–33916, https://doi.org/10.1021/acsami.4c05112.

38. N. Gogurla, S. P. Mondal, A. K. Sinha, et al., "Transparent and Flexible Resistive Switching Memory Devices With a Very High ON/OFF Ratio Using Gold Nanoparticles Embedded in a Silk Protein Matrix," *Nanotechnology* 24 (2013): 345202, https://doi.org/10.1088/0957-4484/24/34/345202.

39. C. Wang, A. Agrawal, E. Yu, and K. Roy, "Multi-Level Neuromorphic Devices Built on Emerging Ferroic Materials: A Review," *Frontiers in Neuroscience* 15 (2021): 661667, https://doi.org/10.3389/fnins.2021.661667.

40. L. Zhu, C. Y. Zhang, L. Gao, et al., "Molecular Layer Deposition of Biomimetic Amino Acid-based Hybrid Thin Films for Artificial Nociceptors," *Journal of Materials Chemistry C* 13 (2025): 5085–5096, https://doi.org/10.1039/d4tc04258a.

41. A. Heredia, V. Meunier, I. K. Bdikin, et al., "Nanoscale Ferroelectricity in Crystalline $\gamma$-Glycine," *Advanced Functional Materials* 22 (2012): 2996–3003, https://doi.org/10.1002/adfm.201103011.

42. S. Barik, "The Uniqueness of Tryptophan in Biology: Properties, Metabolism, Interactions and Localization in Proteins," *International Journal of Molecular Sciences* 21 (2020): 8776, https://doi.org/10.3390/ijms21228776.

43. S. Khemaissa, S. Sagan, and A. Walrant, "Tryptophan, an Amino-Acid Endowed With Unique Properties and its Many Roles in Membrane Proteins," *Crystals* 11 (2021): 1032, https://doi.org/10.3390/cryst11091032.

44. D. A. Dougherty, "Cation-$\pi$ Interactions Involving Aromatic Amino Acids," *The Journal of Nutrition* 137 (2007): 1504S–1508S, https://doi.org/10.1093/jn/137.6.1504S.

45. K. Y. Baek, Y. Fujimura, M. Hayashi, S. H. Lin, and S. K. Kim, "Density Functional Theory Study of Conformation-Dependent Properties of Neutral and Radical Cationic L-tyrosine and L-tryptophan," *The Journal of Physical Chemistry A* 115 (2011): 9658–9668, https://doi.org/10.1021/jp200826z.

46. A. Piatkivskyi, S. Osburn, K. Jaderberg, et al., "Structure and Reactivity of the Distonic and Aromatic Radical Cations of Tryptophan," *Journal of the American Society for Mass Spectrometry* 24 (2013): 513–523, https://doi.org/10.1007/s13361-013-0594-0.

47. L. Mahmoudi, R. Kissner, T. Nauser, and W. H. Koppenol, "Electrode Potentials of L-tryptophan, L-tyrosine, 3-nitro-L-tyrosine, 2,3-difluoro-L-tyrosine, and 2,3,5-trifluoro-L-tyrosine," *Biochemistry* 55 (2016): 2849–2856, https://doi.org/10.1021/acs.biochem.6b00019.

48. S. Goswami, A. J. Matula, S. P. Rath, et al., "Robust Resistive Memory Devices Using Solution-Processable Metal-Coordinated azo aromatics," *Nature Materials* 16 (2017): 1216–1224, https://doi.org/10.1038/nmat5009.

49. B. Das and H. K. Srivastava, "Influence of the Local Chemical Environment in the Formation of Multicomponent Crystals of L-tryptophan With N-heterocyclic Carboxylic Acids: Unusual Formation of Double Zwitterions," *Crystal Growth & Design* 17 (2017): 3796–3805, https://doi.org/10.1021/acs.cgd.7b00386.

50. J. Geng, K. Dornevil, V. L. Davidson, and A. Liu, "Tryptophan-Mediated Charge-Resonance Stabilization in the Bis-Fe(IV) Redox State of MauG," *Proceedings of the National Academy of Sciences* 110 (2013): 9639–9644, https://doi.org/10.1073/pnas.1301544110.

51. A. Aziz, N. A. Abdullah, N. A. M. Asib, R. Mohamed, M. Rusop, and Z. Khusaimi, "Surface Morphology Studies on Different Layers of PMMA Spin Coated Onto Substrate Prepared by Sol-gel Spin-Coating Method," *Advanced Materials Research* 1109 (2015): 608–612, https://doi.org/10.4028/www.scientific.net/AMR.1109.608.

52. S. E. Fritz, T. W. Kelley, and C. D. Frisbie, "Effect of Dielectric Roughness on Performance of Pentacene TFTs and Restoration of Performance With a Polymeric Smoothing Layer," *The Journal of Physical Chemistry B* 109 (2005): 10574–10577, https://doi.org/10.1021/jp044318f.

53. Y. Jin, Z. Rang, M. I. Nathan, P. P. Ruden, C. R. Newman, and C. D. Frisbie, "Pentacene Organic Field-Effect Transistor on Metal Substrate With Spin-Coated Smoothing Layer," *Applied Physics Letters* 85 (2004): 4406–4408, https://doi.org/10.1063/1.1814802.

54. J. Hu, J. Zhang, Z. Fu, et al., "Fabrication of Electrically Bistable Organic Semiconducting/Ferroelectric Blend Films by Temperature Controlled Spin Coating," *ACS Applied Materials & Interfaces* 7 (2015): 6325–6330, https://doi.org/10.1021/acsami.5b00705.

55. J. H. Lee, Y. S. Rim, W. K. Min, et al., "Biocompatible and Biodegradable Neuromorphic Device Based on Hyaluronic Acid for Implantable Bioelectronics," *Advanced Functional Materials* 31 (2021): 2107074, https://doi.org/10.1002/adfm.202107074.

56. D. H. Choi, H. T. Kim, Y. Kim, et al., "Nature-Derived, Biocompatible Silibinin Based Bioresorbable Neuromorphic Device for Implantable Medical Electronics," *Applied Surface Science* 621 (2023): 156814, https://doi.org/10.1016/j.apsusc.2023.156814.

57. K. Moon, S. M. Rho, B. Kim, et al., "Biocompatible Neuromorphic Device Array Based on Naturally Sourced Mucin for Implantable Bioelectronics," *ACS Nano* 19 (2025): 10400–10411, https://doi.org/10.1021/acsnano.4c18846.

58. Q. Li and N. J. Bjerrum, "Aluminum as Anode for Energy Storage and Conversion: A Review," *Journal of Power Sources* 110 (2002): 1–10, https://doi.org/10.1016/S0378-7753(01)01014-X.

59. P. Chen, J. Chen, Q. Zheng, et al., "Enhancing the Performance of Aluminum Anodes in Aqueous Batteries: A Review on Alloying, Microstructure, and Corrosion Inhibition Strategies," *Sustainability* 17 (2025): 9220, https://doi.org/10.3390/su17209220.

60. E. Hoque, J. A. DeRose, G. Kulik, P. Hoffmann, H. J. Mathieu, and B. Bhushan, "Alkylphosphonate Modified Aluminum Oxide Surfaces," *The Journal of Physical Chemistry B* 110 (2006): 10855–10861, https://doi.org/10.1021/jp061327a.

61. K. Y. Cheong, I. A. Tayeb, F. Zhao, and J. M. Abdullah, "Review on Resistive Switching Mechanisms of Bio-Organic Thin Film for Non-Volatile Memory Application," *Nanotechnology Reviews* 10 (2021): 680–709, https://doi.org/10.1515/ntrev-2021-0047.



16163028, 2026, 92, Downloaded from https://advanced.onlinelibrary.wiley.com/doi/10.1002/adfm.78971 by Yonsei University Library, Wiley Online Library on [22/11/2026]. See the Terms and Conditions (https://onlinelibrary.wiley.com/terms-and-conditions) on Wiley Online Library for rules of use; OA articles are governed by the applicable Creative Commons License

62. Y. Xia, W. He, L. Chen, X. Meng, and Z. Liu, "Field-Induced Resistive Switching Based on Space-Charge-Limited Current," *Applied Physics Letters* 90 (2007): 022907, https://doi.org/10.1063/1.2430912.

63. P. Jetty, U. M. Kannan, and S. Jammalamadaka, "Aloe Vera-Inspired Cognitive Computing: Unveiling the Power of Pavlovian Conditioning and Pattern Recognition With a Synaptic RRAM Device," *ACS Applied Electronic Materials* 6 (2024): 1992–2002, https://doi.org/10.1021/acsaelm.4c00023.

64. M. S. Ravisankar, "Study of Electrical Transport and High Voltage Resistive Switching on Ag/PVDF-Fibres/ag and Ag/PVDF-Pellet/Ag for Memory Applications," *Inorganic Chemistry Communications* 158 (2023): 111677, https://doi.org/10.1016/j.inoche.2023.111677.

65. F. Verbakel, S. C. J. Meskers, R. A. J. Janssen, et al., "Reproducible Resistive Switching in Nonvolatile Organic Memories," *Applied Physics Letters* 91 (2007): 192103, https://doi.org/10.1063/1.2806275.

66. B. F. Bory, P. R. F. Rocha, H. L. Gomes, D. M. de Leeuw, and S. C. J. Meskers, "Unipolar Resistive Switching in Metal Oxide/Organic Semiconductor Non-Volatile Memories as a Critical Phenomenon," *Journal of Applied Physics* 118 (2015): 205503, https://doi.org/10.1063/1.4936349.

67. S. P. Park, H. J. Kim, J. H. Lee, and H. J. Kim, "Glucose-Based Resistive Random Access Memory for Transient Electronics," *Journal of Information Display* 20 (2019): 231–237, https://doi.org/10.1080/15980316.2019.1664650.

68. V. M. Le Corre, E. A. Duijnstee, O. El Tambouli, et al., "Revealing Charge Carrier Mobility and Defect Densities in Metal Halide Perovskites via Space-Charge-Limited Current Measurements," *ACS Energy Letters* 6 (2021): 1087–1094, https://doi.org/10.1021/acsenergylett.0c02599.

69. E. Douvogianni, X. Qiu, L. Qiu, et al., "Soft Nondamaging Contacts Formed From Eutectic Ga–In for the Accurate Determination of Dielectric Constants of Organic Materials," *Chemistry of Materials* 30 (2018): 5527–5533, https://doi.org/10.1021/acs.chemmater.8b02212.

70. M. Zhang, W. Qiu, R. Zhang, K. H. Row, Y. Cheng, and Y. Jin, "Effect of Amino Acids on Microwave Dielectric Properties of Minced Antarctic Krill (Euphausia superba)," *Food and Bioprocess Technology* 10 (2017): 1809–1823, https://doi.org/10.1007/s11947-017-1952-x.

71. S. G. Bratsch, "Standard Electrode Potentials and Temperature Coefficients in Water at 298.15 K," *Journal of Physical and Chemical Reference Data* 18 (1989): 1–21, https://doi.org/10.1063/1.555839.

72. P. W. Atkins, *Physical Chemistry*, 6th ed. (Oxford University Press, 1998).

73. H. Abbas, A. Ali, J. Jung, et al., "Reversible Transition of Volatile to Non-Volatile Resistive Switching and Compliance Current-Dependent Multistate Switching in IGZO/MnO RRAM Devices," *Applied Physics Letters* 114 (2019): 093503, https://doi.org/10.1063/1.5082901.

74. U. Celano, L. Goux, A. Belmonte, et al., "Three-Dimensional Observation of the Conductive Filament in Nanoscaled Resistive Memory Devices," *Nano Letters* 14 (2014): 2401–2406, https://doi.org/10.1021/nl500049g.

75. J. Lei, S. Sun, Y. Li, et al., "Electrochemical Resistive Switching in Nanoporous Hybrid Films by One-Step Molecular Layer Deposition," *The Journal of Physical Chemistry Letters* 14 (2023): 1389–1394, https://doi.org/10.1021/acs.jpclett.2c03850.

76. L. Wang, Y. Wang, and D. Wen, "Switching-Enhanced RRAM for Reliable Synaptic Simulation and Multilevel Data Storage," *Journal of Alloys and Compounds* 892 (2021): 162180, https://doi.org/10.1016/j.jallcom.2021.162180.

77. H.-L. Chu, S.-C. Chiu, C.-F. Sung, et al., "Programmable Redox State of the Nickel Ion Chain in DNA," *Nano Letters* 14 (2014): 1026–1031, https://doi.org/10.1021/nl404601s.

78. K. C. Chang, R. Zhang, and T. C. Chang, "High Performance, Excellent Reliability Multifunctional Graphene Oxide Doped Memristor Achieved by Self-Protective Compliance Current Structure," in *2014 IEEE International Electron Devices Meeting (IEDM)* (IEEE, 2014), https://doi.org/10.1109/IEDM.2014.7047161.

79. S. Saini, A. Dwivedi, A. Lodhi, A. Khandelwal, and S. P. Tiwari, "Multilevel Resistive Switching in Flexible RRAM Devices With a PVP:$MoSe_2$ Active Layer," *ACS Applied Electronic Materials* 6 (2024): 6718–6725, https://doi.org/10.1021/acsaelm.4c01130.

80. H. Patil, H. Kim, S. Rehman, et al., "Stable and Multilevel Data Storage Resistive Switching of Organic Bulk Heterojunction," *Nanomaterials* 11 (2021): 359, https://doi.org/10.3390/nano11020359.

81. Y. Liu, Y. Cai, Q. Li, Y. Pan, Z. Wang, and R. Huang, "Inorganic-Organic Hybrid Resistive Switching Memory With High Uniformity and Multilevel Operation," in *2014 International Symposium on VLSI Technology, Systems and Application (VLSI-TSA)* (IEEE, 2014), https://doi.org/10.1109/VLSI-TSA.2014.6839676.

82. C. Zhang, J. Shang, W. Xue, et al., "Convertible Resistive Switching Characteristics Between Memory Switching and Threshold Switching in a Single Ferritin-Based Memristor," *Chemical Communications* 52 (2016): 4828–4831, https://doi.org/10.1039/c6cc00989a.

83. S. A. Khan, M. K. Rahmani, M. U. Khan, J. Kim, J. Bae, and M. H. Kang, "Multistate Resistive Switching With Self-Rectifying Behavior and Synaptic Characteristics in a Solution-Processed ZnO/PTAA Bilayer Memristor," *Journal of The Electrochemical Society* 169 (2022): 063517, https://doi.org/10.1149/1945-7111/ac7754.

84. Z. X. Lim, I. A. Tayeb, Z. A. A. Hamid, et al., "Switching Dynamics and Conductance Quantization of $Aloe$ Polysaccharides-Based Device," *IEEE Transactions on Electron Devices* 66 (2019): 3110–3117, https://doi.org/10.1109/TED.2019.2915106.

85. I. A. Tayeb, F. Zhao, J. M. Abdullah, and K. Y. Cheong, "Resistive Switching Behaviour in a Polymannose Film for Multistate Non-Volatile Memory Application," *Journal of Materials Chemistry C* 9 (2021): 1437–1450, https://doi.org/10.1039/d0tc04655h.

86. J. Park and S. Kim, "Improving Endurance and Reliability by Optimizing the Alternating Voltage in Pt/ZnO/TiN RRAM," *Results in Physics* 39 (2022): 105731, https://doi.org/10.1016/j.rinp.2022.105731.

87. K. Park and J. S. Lee, "Reliable Resistive Switching Memory Based on Oxygen-Vacancy-Controlled Bilayer Structures," *RSC Advances* 6 (2016): 21736–21741, https://doi.org/10.1039/c6ra00798h.

88. T.-M. Tsai, C.-H. Wu, K.-C. Chang, et al., "Controlling the Degree of Forming Soft-Breakdown and Producing Superior Endurance Performance by Inserting BN-Based Layers in Resistive Random Access Memory," *IEEE Electron Device Letters* 38 (2017): 445–448, https://doi.org/10.1109/LED.2017.2664881.

## Supporting Information

Additional supporting information can be found online in the Supporting Information section.

**Supporting File**: adfm78971-sup-0001-SuppMat.docx.



16163028, 2026, 92, Downloaded from https://advanced.onlinelibrary.wiley.com/doi/10.1002/adfm.78971 by Yonsei University Library, Wiley Online Library on [22/11/2026]. See the Terms and Conditions (https://onlinelibrary.wiley.com/terms-and-conditions) on Wiley Online Library for rules of use; OA articles are governed by the applicable Creative Commons License